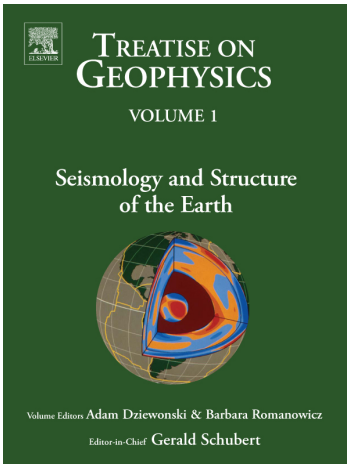
Provided for non-commercial research and educational use.
Not for reproduction, distribution or commercial use.

This article was originally published in the Treatise on Geophysics, published by Elsevier and the attached copy is provided by Elsevier for the author's benefit and for the benefit of the author's institution, for non-commercial research and educational use including use in instruction at your institution, posting on a secure network (not accessible to the public) within your institution,



and providing a copy to your institution's administrator.

All other uses, reproduction and distribution, including without limitation commercial reprints, selling or licensing copies or access, or posting on open internet sites are prohibited. For exceptions, permission may be sought for such use through Elsevier's permissions site at:

http://www.elsevier.com/locate/permissionusematerial

Information taken from the copyright line. The Editor-in-Chief is listed as Gerald Schubert and the imprint is Academic Press.

Author's personal copy

1.16 Deep Earth Structure – Upper Mantle Structure: Global Isotropic and Anisotropic Elastic Tomography

J-P. Montagner, Institut de Physique du Globe, Paris, France

© 2007 Elsevier B.V. All rights reserved.

1.16.1	**Introduction**	559
1.16.2	**Effects of Seismic Velocity and Anisotropy on Seismograms**	560
1.16.2.1	First-Order Perturbation Theory	560
1.16.2.2	Effect of Anisotropic Heterogeneities on Normal Modes and Surface Waves	562
1.16.2.3	Comparison between Surface Wave Anisotropy and SKS Splitting Data	564
1.16.3	**Upper Mantle Tomography of Seismic Velocity and Anisotropy**	565
1.16.3.1	Forward Problem	565
1.16.3.1.1	Data space: *d*	565
1.16.3.1.2	Parameter space: *p*	568
1.16.3.2	Inverse Problem	568
1.16.3.3	Isotropic and Anisotropic Images of the Upper Mantle	571
1.16.4	**Geodynamic Applications**	573
1.16.4.1	Oceanic Plates	574
1.16.4.2	Continents	576
1.16.4.3	Velocity and Anisotropy in the Transition Zone	577
1.16.5	**Numerical Modeling and Perspectives**	579
References		584

1.16.1 Introduction

The first global isotropic tomographic models of the mantle were published in 1984 (Woodhouse and Dziewonski, 1984; Dziewonski, 1984). Since that time, many new tomographic models were published, and a large family of techniques was made available. This important progress was made possible by the extensive use of computers which can handle very large data sets and by the availability of good quality digital seismograms recorded by broadband seismic networks such as GEOSCOPE (Romanowicz *et al.*, 1984), IRIS (Smith, 1986) and all networks coordinated by the Federation of Digital Seismograph Networks (FDSN); Romanowicz and Dziewonski, 1986). Thanks to the installation of modern digital networks, it is now possible to map the whole Earth from the surface down to its center by seismic tomography. However, most tomographic techniques only make use of travel times or phase information in seismograms and very few use the amplitude, even when seismic waveforms are used (Woodhouse and Dziewonski, 1984; Li and Romanowicz, 1996). Global tomographic models have been improved over years by an increase in the number of data and more importantly by using more general parametrizations, now including anisotropy (radial anisotropy in Nataf *et al.* (1986); general slight anisotropy in Montagner and Tanimoto (1990, 1991)) and to a lesser extent anelasticity (Tanimoto, 1990; Romanowicz, 1990). This chapter is focused on the imaging of large-scale (>1000 km) lateral heterogeneities of velocity and anisotropy in the upper mantle (0–660 km depth) where the lateral resolution is the best, thanks to surface waves providing an almost uniform lateral and azimuthal coverage, particularly below oceanic areas. We will discuss how tomographic imaging completely renewed our vision of upper mantle dynamics. It makes it possible to relate surface geology and plate tectonics to underlying mantle convection, and to map at depth the origin of geological objects such as continents, mountain ranges, slabs, ridges, and plumes. The goal of this chapter is not to review all contributions to this topic, but to underline the main scientific issues, to present different approaches and to illustrate the different progress (partly subjectively) by some of our results or by other more recent models. This chapter aims to

Treatise on Geophysics, vol. 1, pp. 559-589

Author's personal copy

show why a major step, which takes a complete account of amplitude anomalies in the most general case and which will enable to map shorter scale heterogeneities, is now possible and presently ongoing.

1.16.2 Effects of Seismic Velocity and Anisotropy on Seismograms

For theoretical and practical reasons, the Earth was considered, for a long time, as composed of isotropic and laterally homogeneous layers. While an isotropic elastic medium can be described by two independent elastic parameters (λ and μ, the Lamé parameters), the cubic symmetry requires three parameters, but the most commonly used anisotropic medium (transverse isotropy with vertical symmetry axis) necessitates five independent parameters (Love, 1927: Anderson, 1961) and the most general elastic medium requires 21 independent parameters. However, since the 1960s, it was recognized that most parts of the Earth are not only laterally heterogeneous but also anisotropic. Though the lateral heterogeneities of seismic velocities were used for a long time for geodynamical applications, the importance of anisotropy for understanding geodynamic processes has only been recognized recently.

Seismology is an observational field based on the exploitation of seismic recordings of the displacement (velocity or acceleration) of the Earth induced by earthquakes. Broadband three-component high dynamic seismometers have been installed in more than 500 stations around the world during the last 20 years (*see* Chapter 1.01). Thanks to progress in instrumentation and theoretical developments, it is now possible to observe and to take a simultaneous account of the effects of lateral heterogeneities of velocity and anisotropy on seismograms.

1.16.2.1 First-Order Perturbation Theory

The basic equation which governs the displacement $\mathbf{u}(\mathbf{r}, t)$ is the elasto-dynamics equation:

$$\rho_0 \frac{\mathrm{d}^2 u_i}{\mathrm{d}t^2} = \sum_j \sigma_{ij,\,j} + F_{\mathrm{I}i} + F_{\mathrm{E}i} \qquad [1]$$

$F_{\mathrm{I}i}$ et $F_{\mathrm{E}i}$ represent, respectively, the whole ensemble of applied inertial and external forces (see Takeuchi and Saito (1972) or Woodhouse and Dahlen (1978) for a complete description of all terms). Generally, by neglecting the advection term, this equation is written in a simple way:

$$(\rho_0 \partial_{tt} - H_0)\mathbf{u}(\mathbf{r},\, t) = \mathbf{F}(\mathbf{r}_{\mathrm{S}},\, t) \qquad [2]$$

where H_0 is an integrodifferential operator and $\mathbf{F}$ expresses all forces applied to the source volume in $\mathbf{r}_{\mathrm{S}}$ at time t (considered as external forces). $\mathbf{F}$ is assumed to be equal to 0 for $t < 0$. In the elastic case, there is a linear relationship between σ_{ij} and the strain tensor ϵ_{kl}: $\sigma_{ij} = \Sigma_{kl}\, \Gamma_{ijkl}\epsilon_{kl}$ (+ terms related to the initial stress). Γ_{ijkl} is a fourth-order tensor, often written in its condensed form C_{ij} as a 6×6 matrix. By using the different symmetry conditions $\Gamma_{ijkl} = \Gamma_{jikl} = \Gamma_{ijlk} = \Gamma_{klij}$, the tensor Γ is shown to have 21 independent elastic moduli in the most general anisotropic medium. In an isotropic medium, this number reduces to two, the Lamé coefficients λ and μ.

When solving for the free oscillations of the Earth, $\mathbf{F} = 0$. The solution $\mathbf{u}(\mathbf{r}, t)$ of eqn [2] can be calculated for a spherically symmetric nonrotating reference Earth model associated with the operator H_0, according to the equation

$$\rho_0 \partial_{tt}\mathbf{u}(\mathbf{r},\, t) = H_0\mathbf{u}(\mathbf{r},\, t) \qquad [3]$$

The solution of eqn [3] is beyond the scope of this chapter and is described in Chapter 1.02. The eigenvalues of the operator H_0 are equal to $-\rho_{0n}\omega_l^2$, where ${}_n\omega_l$ is the eigenfrequency characterized by two quantum numbers n and l, respectively termed radial and angular orders. The corresponding eigenfunctions ${}_n\mathbf{u}_l^m(\mathbf{r}, t)$ depend on three quantum numbers n, l, m, where m is the azimuthal order, with the property that $-l \leq m \leq l$. Therefore, for a given eigenfrequency ${}_n\omega_l$ calculated in a spherically symmetric Earth model, $2l+1$ eigenfunctions can be defined. The eigenfrequency ${}_n\omega_l$ is said to be degenerate, with a degree of degeneracy $2l+1$. There is a complete formal similarity with the calculation of the energy levels of the atom of hydrogen in quantum mechanics. The eigenfunctions ${}_n\mathbf{u}_l^m(\mathbf{r}, t)$ of the operator H_0 are orthogonal and normalized.

The important point is that the basis of functions ${}_n\mathbf{u}_l^m(\mathbf{r}, t)$ is complete. This implies that any displacement at the surface of the Earth can be expressed as a linear combination of these eigenfuctions:

$$\mathbf{u}(\mathbf{r},\, t) = \sum_{n,\,l,\,m} {}_n a_l^m\, {}_n\mathbf{u}_l^m(\mathbf{r},\, t)$$

Author's personal copy

Therefore, these eigenfunctions can be used to calculate the synthetic displacement at any point $\mathbf{r}$, at time t, due to a force system $\mathbf{F}$ in the source volume. For a point force $\mathbf{F}$ at point $\mathbf{r}_S$, a step time function and its associated moment tensor $\mathbf{M}$, which is a good starting model for earthquakes, the solution of eqn [2] is given by (Gilbert, 1971)

$$\mathbf{u}(\mathbf{r},\, t) = \sum_{n,\, l,\, m} {}_n\mathbf{u}_l^m(\mathbf{r}) \frac{(1-\cos {}_n\omega_l t)}{{}_n\omega_l^2} \times \mathrm{e}^{-{}_n\omega_l t/2Q} \left(\mathbf{M} : {}_n\epsilon_l^m\right)_{\mathbf{r}_s} \quad [4]$$

where ϵ is the deformation tensor. Since eqn [4] is linear in $\mathbf{M}$, it can be easily generalized to more complex spatial and temporal source functions, and can be rewritten as

$$\mathbf{u}(\mathbf{r},\, t) = \mathbf{G}(\mathbf{r},\, \mathbf{r}_S,\, t,\, t_S)\mathbf{M}(\mathbf{r}_S,\, t_S)$$

where $\mathbf{G}(\mathbf{r},\, \mathbf{r}_S,\, t,\, t_S)$ is the Green operator of the medium. Normal mode theory is routinely used to calculate synthetic seismograms at long periods ($T \geq 40\,s$.) and centroid moment tensor solutions (Dziewonski *et al.*, 1981).

An example of real and synthetic seismograms is presented in **Figure 1**. However, there are still some discrepancies (usually frequency dependent) between the observed and synthetic seismograms. The simplest way to explain the observed phase shifts (time delays) is to remove the assumption that the Earth is spherically symmetric, that is, there are lateral heterogeneities between the source and the receiver. The next step is to characterize these lateral heterogeneities. Since the agreement between synthetic and observed seismograms is good at long periods ($T \geq 40\,s$), we can reasonably infer that the amplitude of heterogeneities is small (<10%). Behind

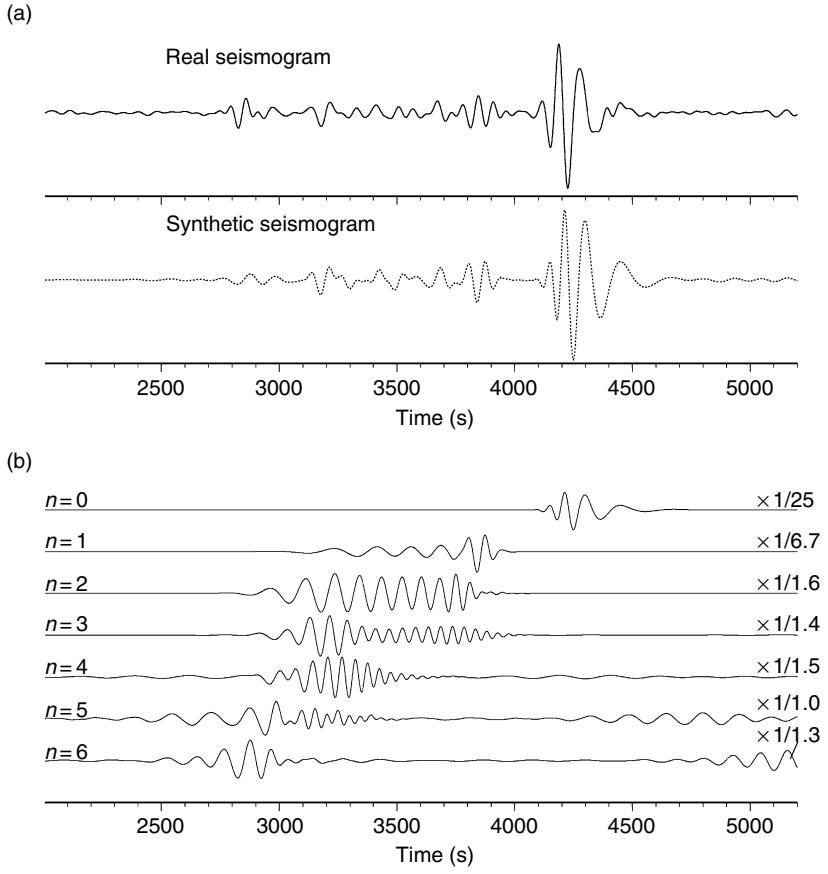


Figure 1 (a) Example of real and synthetic seismograms used for retrieving Rayleigh wave dispersion curve for the fundamental mode and overtones (Beucler *et al.*, 2003). Behind body waves, the signal is composed of surface waves. (b) The complex phase before the high amplitude wave packet corresponding to the fundamental mode of Rayleigh wave (n=0) can be synthetized by summing the first overtones.

Author's personal copy

the surface wave train, a long coda is usually observed, interpreted as scattered waves. However, when filtering out periods shorter than 40 s, this coda vanishes, which means that the scattering effect is only large in the shallowest regions of the Earth (primarily the crust, and the upper lithosphere) but that it is probably negligible at larger depths. However, some groups are starting to use the information contained in these coda waves (Aki and Richards, 1980; Snieder *et al.*, 2002), and even from seismic noise (Shapiro *et al.*, 2005) for imaging the crust. For the sake of simplicity, our study is limited to long-period surface waves and it is hypothesized that the scale of lateral heterogeneities is large compared with the seismic wavelength. This point will be discussed in Section 1.16.3.1. A second hypothesis that must be discussed is the isotropic nature of the Earth materials. Actually, it is a poor assumption, because seismic anisotropy can be unequivocally observed at different scales. Finally, the influence of lateral variations in attenuation must also be taken into account and will be discussed elsewhere in this treatise.

1.16.2.2 Effect of Anisotropic Heterogeneities on Normal Modes and Surface Waves

Different geophysical fields are involved in the investigation of the manifestations of anisotropy of Earth materials: mineral physics and geology for the study of the microscopic scale, and seismology for scales larger than, typically, 1 km. The different observations related to anisotropy, at different scales are reviewed in Montagner (1998) and in Chapter 1.09.

Different kinds of observations have been used for investigating anisotropy in the upper mantle: the Rayleigh–Love wave discrepancy (Anderson, 1961), the azimuthal variation of phase velocities of surface waves (Forsyth, 1975) and the shear-wave splitting particularly for SKS waves (Vinnik *et al.*, 1992). The lack of stations in oceanic areas explains why it is necessary to use surface waves to investigate upper mantle structure (isotropic or anisotropic) at the global or regional scales.

In the simplest case (fundamental modes, no coupling between branches of Rayleigh and Love waves), the frequency shift $\delta\omega/\omega$ (and the corresponding phase velocity perturbation $\delta V/V$), for a constant wavenumber k can be written by applying Rayleigh's principle:

$$\left.\frac{\delta\omega}{\omega}\right|_k = \left.\frac{\delta V}{V}\right|_k = \frac{1}{2\omega}\frac{\int_\Omega \epsilon_{ij}^{*}\,\delta\Gamma_{ijkl}\epsilon_{kl}\,\mathrm{d}\Omega}{\int_\Omega \rho_{0n}\mathbf{u}_l^{m*}{}_n\mathbf{u}_l^m\,\mathrm{d}\Omega} \qquad [5]$$

where ϵ_{ij} and $\delta\Gamma_{ijkl}$ are, respectively, the deformation and the deviations of elastic tensor components from a spherically symmetric, nonrotating, elastic, isotropic (SNREI) model, and ${}_n\mathbf{u}_l^m$ the eigenfunctions as defined in the previous section.

We only consider the propagation of surface waves in a plane-layered medium for a general slight elastic anisotropy, but it can be easily extended to the spherical Earth (Mochizuki, 1986; Tanimoto, 1986; Romanowicz and Snieder, 1988; Larson *et al.*, 1998; Trampert and Woodhouse, 2003). Smith and Dahlen (1973, 1975) found that, to first order in anisotropy and at frequency ω, the azimuthal variation of local phase velocity (Rayleigh or Love wave) can be expanded as a Fourier series of the azimuth Ψ along the path and is of the form

$$\begin{aligned} V(\omega,\theta,\phi,\Psi) - V_0(\omega) = {} & \alpha_0(\omega,\theta,\phi) \\ & + \alpha_1(\omega,\theta,\phi)\cos 2\Psi \\ & + \alpha_2(\omega,\theta,\phi)\sin 2\Psi \\ & + \alpha_3(\omega,\theta,\phi)\cos 4\Psi \\ & + \alpha_4(\omega,\theta,\phi)\sin 4\Psi \end{aligned} \qquad [6]$$

where $V_0(\omega)$ is the reference velocity of the unperturbed medium, and Ψ is the azimuth along the path with respect to the north direction. Montagner and Nataf (1986) present the expressions for the different azimuthal coefficients $\alpha_i(\omega,\theta,\phi)$ as depth integral functions dependent on 13 simple linear combinations of standard cartesian elastic coefficients C_{ij}. Appendix 1 shows how to relate Γ_{ijkl} to C_{ij} and presents detailed calculation of azimuthal terms for Love waves in the geographical coordinate system:

- Constant term (0Ψ-azimuthal term: α_0)

$$A = \rho V_{\mathrm{PH}}^2 = \frac{3}{8}(C_{11}+C_{22}) + \frac{1}{4}C_{12} + \frac{1}{2}C_{66}$$

$$C = \rho V_{\mathrm{PV}}^2 = C_{33}$$

$$F = \frac{1}{2}(C_{13}+C_{23})$$

$$L = \rho V_{\mathrm{SV}}^2 = \frac{1}{2}(C_{44}+C_{55})$$

$$N = \rho V_{\mathrm{SH}}^2 = \frac{1}{8}(C_{11}+C_{22}) - \frac{1}{4}C_{12} + \frac{1}{2}C_{66}$$

Author's personal copy

- 2Ψ-azimuthal term:

$$\alpha_1 \cos 2\Psi \qquad \alpha_2 \sin 2\Psi$$

$$B_c = \frac{1}{2}(C_{11} - C_{22}) \quad B_s = C_{16} + C_{26}$$

$$G_c = \frac{1}{2}(C_{55} - C_{44}) \quad G_s = C_{54}$$

$$H_c = \frac{1}{2}(C_{13} - C_{23}) \quad H_s = C_{36}$$

- 4Ψ-azimuthal term:

$$\alpha_3 \cos 4\Psi \qquad \alpha_4 \sin 4\Psi$$

$$E_c = \frac{1}{8}(C_{11} + C_{22}) + \frac{1}{4}C_{12} - \frac{1}{2}C_{66} \quad E_s = \frac{1}{2}(C_{16} - C_{26})$$

where indices 1 and 2 refer to horizontal coordinates (1: North; 2: East) and index 3 refers to vertical coordinate. ρ is the density, V_{PH}, V_{PV} are respectively horizontally and vertically 'propagating' P-wave velocities, V_{SH}, V_{SV} horizontal and vertical 'polarized' S-wave velocities. So, the different parameters present in the different azimuthal terms are simply related to elastic moduli C_{ij}.

From a practical point of view, once source phase is removed and assuming that the scale of heterogeneities is larger than the wavelength, the total phase ϕ_t (and the travel time) between the epicenter E and the receiver R is easily related to the measurement of phase velocity $V_d(\omega)$, and therefore to the local phase velocity $V(\omega, \theta, \phi, \Psi)$:

$$\phi_t = \omega t_{E\to R} = \frac{\omega\Delta}{V_d(\omega)} = \omega \int_E^R \frac{ds}{V(\omega, \theta, \phi, \Psi)} \qquad [7]$$

Therefore, eqns [6] and [7] define the forward problem in the framework of first-order perturbation theory. We will see in the next section how to solve the inverse problem. This means that, ideally, surface waves in the plane case have the ability to provide information on 13 elastic parameters, which emphasizes the enormous potential of surface waves in terms of geodynamical and petrological implications. There are only 13 elastic moduli among 21, since propagation of surface waves is invariant against rotation by π, which corresponds to a monoclinic symmetry.

The 0-Ψ term corresponds to the average over all azimuths and involves five independent parameters, *A*, *C*, *F*, *L*, *N*, which represent the equivalent transversely isotropic medium with a vertical symmetry axis (more simply named VTI or radial anisotropy). It must be noted that it is possible to retrieve the equivalent isotropic shear modulus from these five parameters. By using a Voigt average, the shear modulus μ_{iso} is given by

$$\mu_{iso} = \rho V_{S_{iso}}^2 = \frac{1}{15}(C_{11} + C_{22} + C_{33} - C_{12} - C_{13} - C_{23} + 3C_{44} + 3C_{55} + 3C_{66})$$

According to the expressions of *A*, *C*, *F*, *L*, *N* in terms of elastic moduli, $\mu_{iso} = \frac{1}{15}(C + A - 2F + 6L + 5N)$ So we can see that the equivalent isotropic velocity depends not only on V_{SV} and V_{SH}, but also on P-wave velocity and anisotropy ($\phi = C/A$) and on $\eta = F/(A-2L)$. By rewriting this expression $\mu_{iso} = \frac{1}{15}(C + (1-2\eta)A + (6+4\eta)L + 5N)$, neglecting anisotropy in P-wave ($\phi = 1$) and assuming $\eta = 1$, it is found that $\mu_{iso} = \rho V_{S_{iso}}^2 \approx \frac{2}{3}L + \frac{1}{3}N = \frac{2}{3}\rho V_{SV}^2 + \frac{1}{3}\rho V_{SH}^2$. Naturally, this choice is partly arbitrary, since usually, there is no S-wave anisotropy without P-wave anisotropy. Another way might consist in using correlations between anisotropic parameters for petrological models as derived by Montagner and Anderson (1989a).

The other azimuthal terms (2-Ψ and 4-Ψ) depend on four groups of two parameters, *B*, *G*, *H*, *E*, respectively describing the azimuthal variation of *A*, *L*, *F*, *N*. These simple parameters make it possible to describe in a simple way the two seismically observable effects of anisotropy on surface waves, the 'polarization' anisotropy (Schlue and Knopoff, 1977) and the azimuthal anisotropy (Forsyth, 1975).

Another important point in these expressions is that they provide the partial derivatives for the radial and azimuthal anisotropy of surface waves. The corresponding kernels and their depth dependence are plotted in Montagner and Nataf (1986) (**Figures 14** and **15**). These partial derivatives of the different azimuthal terms with respect to the elastic parameters can be easily calculated by using a radial anisotropic reference Earth model, such as PREM (Dziewonski and Anderson, 1981). The partial derivatives of the eigenperiod ${}_0T_l$ with respect to parameter p, $(p/T)(\partial T/\partial p)$ can easily be converted into phase velocity partial derivatives by using

$$\frac{p}{V}\left(\frac{\partial V}{\partial p}\right)_T = -\frac{V}{U}\frac{p}{T}\left(\frac{\partial T}{\partial p}\right)_k$$

For example, the parameters G_c and G_s have the same kernel as parameter L (related to V_{SV}) as shown by comparing the expressions of R_1, R_2, and R_3 in eqn [29] of Appendix 1. For fundamental modes, the calculation of kernels shows that Love waves are almost insensitive to V_{SV} (**Figure 14**) and Rayleigh

Author's personal copy

waves to V_{SH}. Rayleigh waves are the most sensitive to SV waves. However, as pointed out by Anderson and Dziewonski (1982), the influence of P-waves (through parameters A and C) can be very large in an anisotropic medium. The influence of density is also very large for Love and Rayleigh waves but, as shown by Takeuchi and Saito (1972), it is largely decreased when seismic velocities are inverted for, instead of elastic moduli and density.

1.16.2.3 Comparison between Surface Wave Anisotropy and SKS Splitting Data

It can be noted that some of the linear combinations of elastic moduli C_{ij}, derived from surface waves in the previous section, also come up when considering the propagation of body waves in symmetry planes for a weakly anisotropic medium (see, e.g., Crampin *et al.* (1984)), and their azimuthal dependence

$$\begin{aligned}\rho V_P^2 &= A + B_c\cos 2\Psi + B_s\sin 2\Psi \\ &\quad + E_c\cos 4\Psi + E_s\sin 4\Psi \\ \rho V_{qSH}^2 &= N - E_c\cos 4\Psi - E_s\sin 4\Psi \\ \rho V_{qSV}^2 &= L + G_c\cos 2\Psi + G_s\sin 2\Psi\end{aligned}$$

where V_{qSH} and V_{qSV} correspond, respectively, to quasi-SH and quasi-SV waves.

A global investigation of anisotropy inferred from SKS body wave splitting measurements (delay times and directions of maximum velocities) has been undertaken by different authors (Vinnik *et al.*, 1992; Silver, 1996; Savage, 1999). Unfortunately, most SKS measurements have been done in continental parts of the Earth, and very few in oceans. It turns out that a direct comparison of body wave and surface wave data sets is now possible (Montagner *et al.*, 2000). If the anisotropic medium is assumed to be characterized by a horizontal symmetry axis with any orientation (this is a very strong assumption which can be alleviated as shown by Chevrot *et al.*, 2004), and for a vertically propagating SKS wave, a synthetic data set of SKS delay times and azimuths can be calculated from the global distribution of anisotropy derived from surface waves, by using the following equations:

$$\delta t_{SKS} = \int_0^h dz\sqrt{\frac{\rho}{L}}\left[\frac{G_c(z)}{L(z)}\cos(2\Psi(z)) + \frac{G_s(z)}{L(z)}\sin(2\Psi(z))\right] \quad [8]$$

where δt_{SKS} is the integrated travel time for the depth range 0 to h for a propagation azimuth Ψ, where the anisotropic parameters $G_c(z)$, $G_s(z)$, and $L(z)$ are the anisotropic parameters retrieved from surface waves at different depths. It is remarkable to realize that only the G-parameter (expressing the SV wave azimuthal variation) is present in this equation. From eqn [8], we can infer the maximum value of delay time δt_{SKS}^{max} and the corresponding azimuth Ψ_{SKS}:

$$\delta t_{SKS}^{max} = \sqrt{\left\{\int_0^h dz\sqrt{\frac{\rho}{L}}\frac{G_c(z)}{L(z)}\right\}^2 + \left\{\int_0^h dz\sqrt{\frac{\rho}{L}}\frac{G_s(z)}{L(z)}\right\}^2} \quad [9]$$

$$\tan(2\Psi_{SKS}) = \frac{\int_0^h dz G_s(z)/L(z)}{\int_0^h dz\frac{G_c(z)}{L(z)}} \quad [10]$$

However, eqn [8] is approximate and only valid when the wavelength is much larger than the thickness of layers. It is possible to make more precise calculations by using the technique derived for two layers by Silver and Savage (1994) or by using the general expressions given in Rumpker and Silver (1998), Montagner *et al.* (2000), and Chevrot *et al.* (2004).

With eqns [9] and [10], a synthetic map of the maximum value of delay time δt_{SKS}^{max} can be obtained by using a 3-D anisotropic surface wave model. A detailed comparison between synthetic SKS derived from anisotropic upper mantle (AUM) model (Montagner and Tanimoto, 1991) and observed SKS (Silver, 1996) was presented in Montagner *et al.* (2000). **Figure 2** shows such a map for the Earth

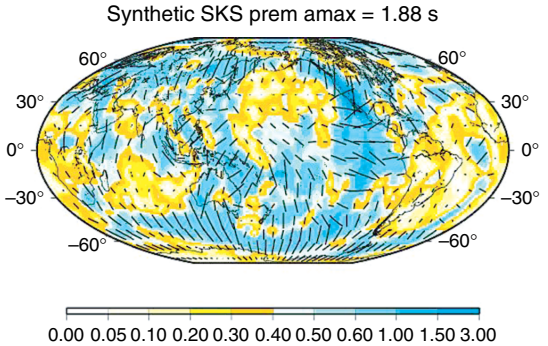


Figure 2 Map of synthetic SKS splitting delay time derived from the anisotropic surface wave model of Montagner (2002). The delay time is expressed in seconds; $A_{max} = 1.88$ s.

Author's personal copy

centered in the Pacific, by using the anisotropic surface wave model of Montagner (2002) derived from the data of Montagner and Tanimoto (1991) and Ekström *et al.* (1997). First of all, the comparison shows that both data sets are compatible in magnitude but not necessarily in directions. Some contradictions between measurements derived from surface waves and from body waves have been noted. The agreement of directions is correct in tectonically active areas but not in old cratonic zones. The discrepancy in these areas results from the rapid lateral change of directions of anisotropy at a small scale. These changes stem from the complex history of these areas, which have been built by successive collages of continental pieces. It might also result from the hypothesis of horizontal symmetry axis, which was shown to be invalid in many areas (Plomerova *et al.*, 1996). The positive consequence of this discrepancy is that a small-scale mapping of fossile anisotropy in such areas might provide clues for understanding the processes of growth of continents and mountain building opening a new field, the paleoseismology.

Unlike surface waves, SKS waves have a good lateral resolution, and are sensitive to the short wavelength anisotropy just below the stations. But their drawback is that they have a poor vertical resolution. On the other hand, global anisotropy tomography derived from surface waves only provides long-wavelength anisotropy (poor lateral resolution) but enables the location at depth of anisotropy. The long-wavelength anisotropy derived from surface waves will display the same direction as the short-wavelength anisotropy inferred from body waves only when large-scale vertical coherent processes are predominant. As demonstrated by Montagner *et al.* (2000), the best agreement between observed and synthetic SKS can be found when only layers in the uppermost 200 km of the mantle are taken into account. Moreover, tomographic models derived from surface waves lose resolution at depths greater than 200 km. In some continental areas, short-scale anisotropy, the result of a complex history, might be important and even might mask the large-scale anisotropy more related to present convective processes (see, e.g., Marone and Romanowicz, 2006 for North America). From a statistical point of view, good agreement is found between orientations of anisotropy and plate velocity motion for fast-moving plates. The differences between anisotropy and tectonic plate directions are related to more complex processes, as will be seen in Section 1.16.3.

1.16.3 Upper Mantle Tomography of Seismic Velocity and Anisotropy

We now show how to implement theory of Section 1.16.1 from a practical but general point of view, and how to design a tomographic technique in order to invert for the 13 different elastic parameters and density. A tomographic technique necessitates solving simultaneously a forward problem and an inverse problem. By using the results of the previous section, it successively considers how to set the forward problem, and how it is used to retrieve a set of parameters by inversion.

1.16.3.1 Forward Problem

First, it is necessary to define the data space **d** and the parameter space **p**. It is assumed that a functional **g** relating **d** and **p** can be found such that

$$\mathbf{d} = \mathbf{g}(\mathbf{p})$$

where **d** is the set of data (which samples the data space), and **p** the set of parameters.

1.16.3.1.1 Data space: d

The basic data set is made of seismograms $\mathbf{u}(t)$. We can try to directly match the waveform in the time domain, or we can work in the Fourier domain, by separating phase and amplitude on each component $u_i(t)$:

$$u_i(t) = \int_{-\infty}^{\infty} A_i(\omega) e^{i(\omega t - \phi_i)} d\omega$$

The approach consisting in fitting seismic waveforms is quite general but, from a practical point of view, it does not necessarily correspond to the simplest choice. In a heterogeneous medium, the calculation of amplitude and phase effects makes it necessary to calculate the coupling between different multiplets (Li and Tanimoto, 1993; Li and Romanowicz, 1995; Marquering *et al.*, 1996), which is very time consuming. When working in Fourier domain, different time windows can be considered and the phase of different seismic trains, body waves and surface waves can be separately matched (Nolet, 1990; Lévêque *et al.*, 1991) under drastic simplifying assumptions. **Figure 1** shows an example of observed and synthetic seismograms, the latter obtained by normal mode summation with the different higher modes. The fundamental wave train is well separated from other

Author's personal copy

modes at large epicentral distances. The part of the seismogram corresponding to higher modes is more complex and shows overlap of these modes in the time domain. Therefore, from a practical point of view, the fitting of the fundamental mode wave train will not cause any problem and has been widely used in global mantle tomography. The use of higher mode wave trains and the separation of overtones is much more difficult. The first attempts were performed by Nolet (1975), Cara (1979), Okal and Jo (1985), and Dost (1990) by applying a spatial filtering method. Unfortunately, all these techniques can only be applied in areas where dense arrays of seismic stations are present, that is, in North America and Europe. By using a set of seismograms recorded at one station but corresponding to several earthquakes located in a small source area, Stutzmann and Montagner (1994) showed how to separate the different higher modes. A similar approach was also followed by Van Heijst and Woodhouse (1997). We only detail in this paper the technique which was designed for fitting the fundamental mode wave train and the reader is referred to Stutzmann and Montagner (1994), Van Heijst and Woodhouse (1997), and Beucler *et al.* (2003) for the description of the recovery of higher-mode dispersion properties and to Romanowicz (2002) for a general overview. **Figure 3** presents an example of phase velocity dispersion for different surface wave modes (fundamental and first higher modes (Beucler *et al.*, 2003)) and how they compare with previous investigations (Cara, 1979; Van Heijst and Woodhouse, 1997).

We take advantage of the fact that, according to the Fermat's principle, the phase velocity perturbation is only dependent to second order on path perturbations, whereas amplitude perturbations are dependent, to first order, on these perturbations, which implies that the eigenfunctions must be recalculated at each iteration. Therefore, the phase is a more robust observable than the amplitude. The amplitude $A(\omega)$ depends in a complex manner on seismic moment tensor, attenuation, scattering, focusing effects, station calibration and near-receiver structure whereas the contribution of lateral heterogeneities of seismic velocity and anisotropic parameters to the phase $\phi(\omega)$ can be easily extracted. The data set under investigation, is composed of propagation times (or phase velocity measurements for surface waves) along paths: $\mathbf{d} = \{\Delta/V(\omega)\}$.

On the other hand, the phase of a seismogram at time t is decomposed, as follows: $\phi = \mathbf{k}\cdot\mathbf{r} + \phi_0^{'}$, where $\mathbf{k}$ is the wave vector, $\phi_0^{'}$ is the initial phase including several terms: $\phi_0^{'} = \phi_0 + \phi_S + \phi_I$, ϕ_S is the initial source phase, ϕ_0 is related to the number of polar phase shifts, ϕ_I is the instrumental phase. ϕ can be measured on seismograms by Fourier

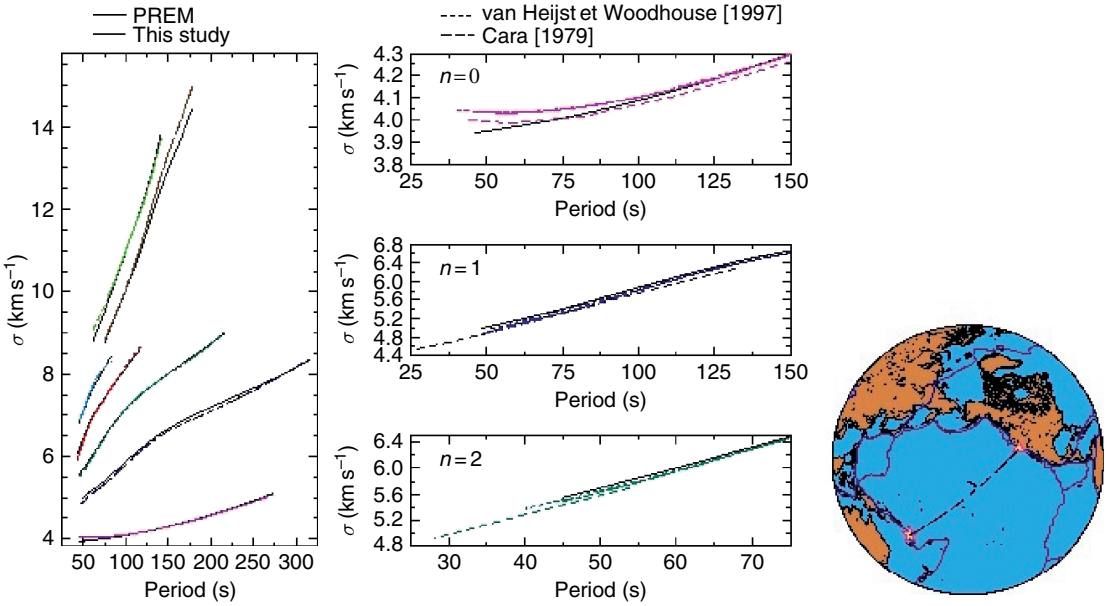


Figure 3 Phase velocity of the fundamental mode and the first six higher modes of Rayleigh compared with PREM (right plot) and with results (center) obtained in previous studies along the same path between Vanuatu and California (SCZ geoscope station) (Beucler *et al*., 2003).

Author's personal copy

transform. We usually assume that ϕ_S is correctly given by the centroid moment tensor solution. For a path between epicenter E and receiver R with an epicentral distance Δ, the phase ϕ is given by

$$\phi = \frac{\omega\Delta}{V_{obs}} + \phi_0 + \phi_S + \phi_I \qquad [11]$$

In the general case, we want to relate the observed phase velocity $V_{obs}(\omega)$ to the parameters of the Earth model $\mathbf{p}(\mathbf{r}, \theta, \phi)$. Data and 3-D parameters can be related through integrals over the whole volume of the Earth. But for computing reasons, it is usual to use a multistep approach, where we first retrieve the local phase velocity $V(\omega, \theta, \phi)$ including its azimuthal terms, and then perform the inversion at depth. These two steps can be reversed since the order of the integrations can be reversed. It is necessary to consider the nature of the perturbed medium. Following the approach of Snieder (1988), if the perturbed medium is at the same time smooth (long-wavelength heterogeneities) and weak (small amplitude of heterogeneities), the geometrical optics approximation (and ray theory) applies. This hypothesis is not necessarily met within the Earth where some geological objects (slabs, mantle plumes, etc.) have a length scale which can be close to the seismic wavelength. In the approximation of ray theory, the volume integral reduces to the curvilinear integral along the geometrical ray path. When ray theory is applicable, we have

$$\phi - \phi_0' = \frac{\omega\Delta}{V_{obs}(\omega)} = \int_E^R \frac{\omega\, ds}{V(\omega, \theta, \phi)} \qquad [12]$$

where the integral is evaluated along the ray path between the epicenter E and the receiver R. Following the results of the previous section, different approximations are implicitly made when using this expression of the phase:

- Large angular order $l \gg 1$, but not too large (scattering problems). From a practical point of view, this means that measurements are performed in the period range $40\,s < T < 200\,s$ with seismic wavelengths between 200 and 1000 km.
- Geometrical optics approximation. If λ is the wavelength of the surface wave at period T, and Λ_S the spatial wavelength of heterogeneity: $\Lambda_S \gg \lambda = VT \Rightarrow \Lambda_S \gtrsim 2000\,km$. Epicentral distance Δ must be larger than seismic wavelength.
- Slight anisotropy and heterogeneity. $\delta V/V \ll 1$. According to Smith and Dahlen (1973) for the plane case, the local phase velocity can be decomposed as a Fourier series of the azimuth Ψ (eqn (6)): Each azimuthal term $\alpha_i(T, \theta, \phi)$ of eqn [6] can be related to the set of parameters $p_i(r, \theta, \phi)$ (density + 13 elastic parameters), according to the expressions derived in Appendix 1:

$$\begin{aligned}\frac{\Delta}{V_{obs}(T)} - \frac{\Delta}{V_0(T)} &= -\sum_{j=0}^{2}\sum_{i=1}^{14}\int_E^R \frac{ds}{V_0}\int_0^a \left[\left(\frac{p_i}{V}\frac{\partial V}{\partial p_i}\right)_j \frac{\delta p_i(r, \theta, \phi)}{p_i}\cos(2j\Psi)\right. \\ &\quad \left. + \left(\frac{p_i}{V}\frac{\partial V}{\partial p_i}\right)_j \frac{\delta p_i(r, \theta, \phi)}{p_i}\sin(2j\Psi)\right] \end{aligned} \qquad [13]$$

Equation [13] defines the forward problem in the framework of first-order perturbation theory, relating the data and the parameter spaces. This approach is usually named path average approximation (PAVA). Many terms in eqn [13] are equal to zero since all parameters are not present in each azimuthal term. A last important ingredient in the inverse problem formulation is the structure of the data space. It is expressed through its covariance function (continuous case) or covariance matrix (discrete case) of data C_d. When data d_i are independent, C_d is diagonal and its elements are the square of the errors on data σ_{d_i}.

1.16.3.1.1.(i) Finite-frequency effects As mentioned previously, a strong hypothesis is that in the framework of geometrical optics approximation, only large-scale heterogeneities can be retrieved. But interesting geological objects such as slabs and plumes are smaller scale. To go beyond the ray theory, it is necessary to take account of the finite-frequency effect when scale length has the same order of magnitude as the seismic wavelength. It is possible to use the scattering theory based on the Born or Rytov approximations (see, e.g., Woodhouse and Girnius (1982) for normal mode approach, Snieder (1988) for surfaces waves, Yomogida (1992), and Dahlen *et al.* (2000) for body waves). Equation [13] shows that the sensitivity kernels are 1-D, meaning that only heterogeneities in the vertical plane containing the source and the receiver are taken into account, whereas, by using the scattering theory, it is possible to calculate 3-D kernels and consequently to take account of off-path

Author's personal copy

heterogeneities. Equations [12] and [13] must be replaced by an integral over the volume Ω:

$$\frac{\Delta}{V_{\text{obs}}(T)} - \frac{\Delta}{V_0(T)} = \sum_{i=1}^{14} \int\int\int_{\Omega} \times K_i(T, \theta, \phi) \frac{\delta p_i(r, \theta, \phi)}{p_i} \mathrm{d}\Omega \qquad [14]$$

where $K(T, \theta, \phi)$ is the scattering Fréchet sensitivity kernel, which depends on wave type (Rayleigh or Love) and on the relative location of E and R (see, e.g., Romanowicz (2002) for a review). Very different strategies can be followed for calculating this triple integral, by separating the surface integral and the radial integral. For a point scatterer, the kernel displays a typical shape of banana-doughnut (Dahlen *et al.*, 2000). Different approximations of $K(T, \theta, \phi)$ have been proposed (Spetzler *et al.*, 2002; Yoshizawa and Kennett, 2002; Ritzwoller *et al.*, 2002), but Sieminski *et al.* (2004) claimed that ray theory surface wave tomography with a very dense path coverage can detect heterogeneities with length scales close and even smaller than the seismic wavelength. The discussion of the advantages and shortcomings of these different techniques is beyond the scope of this chapter, but some new tomographic models using 3-D sensitivity kernels are starting to be constructed (Zhou *et al.*, 2004, 2006) for radially anisotropic media.

1.16.3.1.2 Parameter space: p

It is quite important to consider the structure of the parameter space in detail. First of all, it is necessary to define which parameters are required to explain our data set, how many physical parameters can be effectively inverted for, in the framework of the theory that is considered. For example, if the Earth is assumed to be elastic, laterally heterogeneous but isotropic, only three independent physical parameters, V_P, V_S, and density ρ (or the elastic moduli λ, μ, and ρ) can be inverted for, from surface waves. In a transversely isotropic medium with a vertical symmetry axis (Anderson, 1961; Takeuchi and Saito, 1972), the number of independent physical parameters is now six (five elastic parameters + density). In the most general case of a weak anisotropy, 14 physical parameters (13 combinations of elastic moduli + density) can actually be inverted for, using surface waves. Therefore, the number of 'physical' parameters p_i depends on the underlying theory which is used for explaining the data set.

Once the number of physical independent parameters is defined, we must define how many spatial (or geographical) parameters are required to describe the 3-D distributions $p_i(r, \theta, \phi)$. This is a difficult problem because the number of spatial parameters that can be reliably retrieved from the data set is not necessarily sufficient to provide a correct description of $p_i(r, \theta, \phi)$, that is, of the real Earth. The correct description of $p_i(r, \theta, \phi)$ depends on its spectral content: for example, if $p_i(r, \theta, \phi)$ is characterized by very large wavelengths, only a small number of spatial parameters is necessary, but if $p_i(r, \theta, \phi)$ presents very small scale features, the number of spatial parameters will be very large. In any case, it is necessary to assess the range of possible variations for $p_i(r, \theta, \phi)$ in order to provide some bounds on the parameter space. This is done through a covariance function of parameters in the continuous case (or a covariance matrix for the discrete case) $C_{pipj}(\mathbf{r}, \mathbf{r}')$ at two different points $\mathbf{r}$, $\mathbf{r}'$. These *a priori* constraints can be provided by other fields in geosciences, geology, mineralogy, numerical modeling, etc.

Consequently, a tomographic technique must not be restricted to the inversion of parameters $\mathbf{p} = \{p_i(r, \theta, \phi)\}$ that are searched for, but must include the calculation of the final covariance function (or matrix) of parameters C_p. This means that the retrieval of parameters is contingent to the resolution and the errors of the final parameters and is largely dependent on the resolving power of data (Backus and Gilbert, 1967, 1968, 1970). Finally, the functional $\mathbf{g}$ which expresses the theory relating the data space to the parameter space is also subject to uncertainty. In order to be completely consistent, it is necessary to define the domain of validity of the theory and to assess the error σ_T associated with the theory. Tarantola and Valette (1982) showed that the error σ_T is simply added to the error on data σ_d.

1.16.3.2 Inverse Problem

So far, we did not make assumption on the functional $\mathbf{g}$ relating data and parameters. But in the framework of first-order perturbation theory, the forward problem is usually linearized and eqn [13] can be simply written in the linear case:

$$\mathbf{d} = \mathbf{G}\mathbf{p}$$

where $\mathbf{G}$ is now a matrix (or a linear operator) composed of Fréchet derivatives of $\mathbf{d}$ with respect to $\mathbf{p}$,

Author's personal copy

which has the dimensions $n_d \times n_p$ (number of data $\times$ number of parameters). This matrix usually is not square and many different techniques in the past have been used for inverting $\mathbf{G}$. In any case, the inverse problem will consist in finding an inverse for the functional $\mathbf{g}$, which we will write $\tilde{\boldsymbol{g}}^{-1}$, notwithstanding the way it is obtained, such that

$$\mathbf{p} = \tilde{\boldsymbol{g}}^{-1}(\mathbf{d})$$

To solve the inverse problem, different algorithms can be used. The least-squares solution is usually solved by minimizing a cost function $\mathcal{J}$. Making the data space and the parameter space symmetric, Tarantola and Valette (1982) define the cost function $\mathcal{J}$ as

$$\mathcal{J} = (\mathbf{d}-\mathbf{G}\mathbf{p})^{\mathrm{t}} C_d^{-1}(\mathbf{d}-\mathbf{G}\mathbf{p}) + (\mathbf{p}-\mathbf{p}_0)^{\mathrm{t}} C_p^{-1}(\mathbf{p}-\mathbf{p}_0)$$

The first term corresponds to classical least-squares with no damping, whereas the second term corresponds to norm damping, which imposes smoothness upon the parameter space. Different choices were proposed for this second term. For example, Montagner (1986b) uses a Gaussian covariance function characterized by a correlation length and an *a priori* error σ_p on parameters, whereas Su *et al.* (1984) prefer to minimize the roughness of the model. Other choices consist in taking a constant value such that $\delta\mathbf{p}^{\mathrm{t}} C_p^{-1} \delta\mathbf{p} = \lambda^2 \delta\mathbf{p}^{\mathrm{t}} \delta\mathbf{p}$ (Yoshizawa and Kennett, 2004). Or the covariance operator can be replaced by a Laplacian operator (see, e.g., Zhou *et al.*, 2006):

$$\delta\mathbf{p}^{\mathrm{t}} C_p^{-1} \delta\mathbf{p} = \varepsilon \left(\int\int\int |\nabla^2 \left(\frac{\delta p}{p} \right)|^2 d\Omega \right)^{1/2}$$

A discussion about damping can be found in Trampert and Snieder (1996), who prefer Laplacian over model damping to reduce the spectral leakage.

As an example, by using the expression of $\mathcal{J}$, a quite general and widely used algorithm has been derived by Tarantola and Valette (1982):

$$\begin{aligned} \mathbf{p}-\mathbf{p}_0 &= \left(G^{\mathrm{t}} C_d^{-1} G + C_{p_0}^{-1} \right)^{-1} G^{\mathrm{t}} C_d^{-1} (\mathbf{d}-\mathbf{g}(\mathbf{p}) + G(\mathbf{p}-\mathbf{p}_0)) \\ &= C_{p_0} G^{\mathrm{t}} (C_d + G C_{p_0} G^{\mathrm{t}})^{-1} (\mathbf{d}-\mathbf{g}(\mathbf{p}) \\ &\quad + G(\mathbf{p}-\mathbf{p}_0)) \end{aligned} \qquad [15]$$

where C_d is the covariance matrix of data, C_{p0} the covariance function of parameters $\mathbf{p}$, and G is the Frechet derivative of the operator $\mathbf{g}$ at point $\mathbf{p}(\mathbf{r})$. This algorithm can be made more explicit by writing it in its integral form:

$$\begin{aligned} \mathbf{p}(\mathbf{r}) = \mathbf{p}_0(\mathbf{r}) + \sum_i \sum_j \int_V \mathrm{d}\mathbf{r}'\, C_{p0}(\mathbf{r}, \mathbf{r}') \\ \times G_i(\mathbf{r}')(S^{-1})_{ij} F_j \end{aligned} \qquad [16]$$

with

$$S_{ij} = C_{d_{ij}} + \int_V \mathrm{d}\mathbf{r}_1 \mathrm{d}\mathbf{r}_2 G_i(\mathbf{r}_1) C_{p_0}(\mathbf{r}_1, \mathbf{r}_2) G_j(\mathbf{r}_2)$$

$$F_j = d_j - g_j(\mathbf{p}) + \int_V \mathrm{d}\mathbf{r}'' G_j(\mathbf{r}'')(\mathbf{p}(\mathbf{r}'') - \mathbf{p}_0(\mathbf{r}''))$$

This algorithm can be iterated and is suited for solving slightly nonlinear problems. Different strategies can be followed to invert for the 3-D models $\mathbf{p}(\mathbf{r})$, because the size of the inverse problem is usually enormous in practical applications and a compromise must be found between resolution and accuracy (and also computing time). For the example of mantle tomography, a minimum parameter space will be composed of 13 (+density) physical parameters multiplied by 30 layers (if the mantle is divided into 30 independent layers. If geographical distributions of parameters are searched for up to degree 40 (lateral resolution around 1000 km), this implies a number of $\sim$700 000 independent parameters. Such a problem is still very difficult to handle from a computational point of view. A simple approach for solving this problem consists in dividing the inversion procedure into two steps. The first step consists in regionalizing phase (or group) velocity data in order to retrieve the different azimuthal terms, and the second step is the inversion at depth. It was implemented by Montagner (1986a, 1986b) and a very similar technique is presented by Barmin *et al.* (2001). In case of a large data set, Montagner and Tanimoto (1990) showed how to handle the inverse problem by making a series expansion of the inverse of matrix S. It was recently optimized from a computational point of view by Debayle and Sambridge (2004) and Beucler and Montagner (2006). One advantage of this technique is that it can be applied indifferently to regional studies or global studies. In case of imperfect spatial coverage of the area under investigation, it does not display ringing phenomena commonly observed when a spherical harmonics expansion is used (Tanimoto, 1986).

From a practical point of view, the choice of the model parameterization is also very important and different possibilities can be considered:

- Discrete basis of functions. A simple choice consists in dividing the Earth into 3-D blocks with a surface block size different from the radial one.

Author's personal copy

The size of block depends on the lateral resolution expected from the path coverage. A variant of this parametrization is the use of a set of spherical triangular grid points (see, e.g., Zhou *et al.* (2006)). The block decomposition is valid as well for global investigations as for regional studies. Usually, the Earth surface parametrization is different for the radial one. For global study, the natural basis is composed of the spherical harmonics for the horizontal variations $p_i(r, \theta, \phi) = \sum_{l=0}^{l_{\max}} \sum_{m=-l}^{l} a_l^m(r)\, Y_l^m(\theta, \phi)$. Other choices are possible, such as spherical splines (Wang and Dahlen, 1995). When data coverage is very uneven, other strategies are proposed using irregular cells or adaptative meshes (see, e.g., Zhang and Thurber (2005)).

- Continuous function $\mathbf{p}(\mathbf{r})$. In this case, the function is directly inverted for. Since the number of parameters is then infinite, it is necessary to regularize the solution by defining a covariance function of parameters $C_{p0}(\mathbf{r}, \mathbf{r}')$. For the horizontal variations, a Von Mises distribution (Montagner, 1986b) can be used for initial parameters $\mathbf{P}_0(\mathbf{r})$:

$$C_{p_0}(\mathbf{r}, \mathbf{r}') = \sigma_p(\mathbf{r})\sigma_p(\mathbf{r}') \exp \frac{\cos \Delta_{\mathbf{r}\mathbf{r}'} - 1}{L_{\text{cor}}^2}$$
$$\approx \sigma_p(\mathbf{r})\sigma_p(\mathbf{r}') \exp \frac{-\Delta_{\mathbf{r}\mathbf{r}'}^2}{2L_{\text{cor}}^2}$$

where L_{cor} is the correlation length, which defines the smoothness of the final model. This kind of distribution is well suited for studies on a sphere and is asymptotically equivalent to a Gaussian distribution when $L_{\text{cor}} \ll a$ (a radius of the Earth). When distributions of different azimuthal terms are searched for, it is possible to define cross-correlated covariance functions of parameters $C_{pipj}(\mathbf{r}, \mathbf{r}')$, but since the different terms of the Fourier expansion in azimuth correspond to orthogonal functions, the cross-correlated terms off the diagonal can be taken equal to zero.

It is interesting to note that in eqn [16] the Frechet derivatives G along the path are multiplied by the Gaussian covariance operator C_{p0}. It means that the technique, which can be named Gaussian tomography, is equivalent to use fat rays: when the correlation length is wider than the Fresnel zone, ray theory applies and, consequently, the finite-frequency effects can be neglected. As discussed by Ritzwoller *et al.* (2002) and Sieminski *et al.* (2004), there might be some slight differences in amplitude between Gaussian tomography and diffraction tomography (taking account of finite-frequency effects), but not in the location of heterogeneities provided that the spatial path coverage is sufficiently dense. The radial parametrization must be related to the resolving capability of the data at depth, according to the frequency range under consideration. For the radial variations, polynomial expansions can be used (see, e.g., Dziewonski and Woodhouse (1987) for Tchebyshev polynomials, or Boschi and Ekström (2002) for radial cubic splines). Since the number of physical parameters is very large for the inversion at depth, physical parameters are usually correlated. The different terms of the covariance function C_p between parameters p_1 and p_2 at radii r_i and r_j can be defined as follows:

$$C_{p_1, p_2}(r_i, r_j) = \sigma_{p_1}(r_i)\sigma_{p_2}(r_j)\zeta_{p_1, p_2} \exp\left[-\frac{(r_i - r_j)^2}{2L_{r_i}L_{r_j}}\right]$$

Where $\zeta_{p1,p2}$ is the correlation between physical parameters p_1 and p_2 inferred for instance from different petrological models (Montagner and Anderson, 1989a) such as pyrolite (Ringwood, 1975) and piclogite (Anderson and Bass, 1984; Bass and Anderson, 1986). L_{r_i}, L_{r_j} are the radial correlation lengths, which are used to smooth the inverse model.

The *a posteriori* covariance function is given by

$$C_p = C_{p_0} - C_{p_0} G^T (C_d + G C_{p_0} G^t)^{-1} G C_{p_0}$$
$$= \left(G^T C_d^{-1} G + C_{p_0}^{-1}\right)^{-1} \quad [17]$$

The resolution R of parameters can be calculated as well. It corresponds to the impulsive response of the system: $\mathbf{p} = \tilde{\boldsymbol{g}}^{-1}\ \mathbf{d} = \tilde{\boldsymbol{g}}^{-1}\ \mathbf{gp}' = R\mathbf{p}'$. If the inverse problem is perfectly solved, R is the identity function or matrix. However, the following expression of resolution is only valid in the linear case (Montagner and Jobert, 1981):

$$R = C_{p_0} G^t (C_d + G C_{p_0} G^t)^{-1} G = (G^t C_d G + C_{p_0})^{-1} G^t C_d^{-1} G \quad [18]$$

It is interesting to note that the local resolution of parameters is imposed by both the correlation length and the path coverage, unlike the Backus-Gilbert (1967, 1968) approach, which primarily depends on the path coverage. The effect of a damping factor in the algorithm to smooth the solution is equivalent to the introduction of a simple covariance function on parameters weighted by the errors on data (Ho-Liu *et al.*, 1989). When the correlation length is chosen very small, the algorithms of Backus-Gilbert (1968, 1970) and Tarantola and Valette (1982) are equivalent.

Author's personal copy

By considering the *a posteriori* covariance function and the resolution, it is possible to assess the reliability of the hypotheses made about the independence of parameters. For example, Tanimoto and Anderson (1985) and Montagner and Jobert (1988) showed that there is a tradeoff between azimuthal terms and constant term in case of a poor azimuthal coverage. For the inversion at depth, Nataf *et al.* (1986) also display the tradeoff between physical parameters V_{PH}, V_{SV}, ξ, ϕ, and η when only Rayleigh and Love wave 0-Ψ terms are used in the inversion process.

Though 13 elastic parameters (+ density) are necessary to explain surface wave data (Rayleigh and Love waves), only four parameters are well resolved for small anisotropy (Montagner and Jobert, 1988): the azimuthally averaged S-wave velocity V_S, the radial anisotropy expressed through the ξ parameter ($\xi = (V_{SH}/V_{SV})^2$), where V_{SH} (resp. V_{SV}) is the velocity of S-wave propagating horizontally with horizontal transverse polarization (resp. with vertical polarization), and the $\mathbf{G}$ (G_c, G_s) parameters expressing the horizontal azimuthal variation of V_{SV}. ξ was introduced in the reference Earth model PREM (Dziewonski and Anderson, 1981) down to 220 km in order to explain a large data set of free oscillation eigenfrequencies and body wave travel times. The other elastic parameters can be derived by using constraints from petrology in order to reduce the parameter space (Montagner and Anderson, 1989a). This approach was followed by Montagner and Anderson (1989b) to derive an average reference earth model, and by Montagner and Tanimoto (1991) for the first global 3-D anisotropic model of the upper mantle.

1.16.3.3 Isotropic and Anisotropic Images of the Upper Mantle

The complete anisotropic tomographic procedure has been implemented for making different regional and global studies. Many global isotropic tomographic models of the upper mantle were published since Wooodhouse and Dziewonski (1984) and the recent results have been reviewed by Romanowicz (2003). Many models inverting only for radial anisotropy but neglecting azimuthal anisotropy have also been published (Nataf *et al.*, 1984, 1986; Ekström and Dziewonski, 1998; Shapiro and Ritzwoller, 2002, Gung *et al.*, 2003; Panning and Romanowicz, 2004; Zhou *et al.*, 2006) The complete anisotropic tomographic technique (including azimuthal anisotropy) has been applied for investigating the upper mantle structure either at a regional scale of the Indian Ocean (Montagner, 1986a; Montagner and Jobert, 1988; Debayle and Lévêque, 1997), the Atlantic Ocean (Mocquet and Romanowicz, 1989; Silveira *et al.*, 1998), Africa (Hadiouche *et al.*, 1989; Debayle *et al.*, 2001; Sebai *et al.*, 2005; Sicilia *et al.*, 2005), Pacific Ocean (Nishimura and Forsyth, 1989; Montagner, 2002; Ritzwoller *et al.*, 2004), Antarctica (Roult *et al.*, 1994), Australia (Debayle and Kennett, 2000; Simons *et al.*, 2002), and Central Asia (Griot *et al.*, 1998a, 1998b); Villaseñor *et al.*, 2001) or at a global scale (Montagner and Tanimoto, 1990, 1991; Montagner, 2002; Debayle *et al.*, 2004). The reader is also referred to a quantitative comparison of tomographic and geodynamic models by Becker and Boschi (2002).

An important issue when constructing tomographic models is the correction for crustal structure, where sedimentary thickness and Moho depth variations are so strong that they affect dispersion of surface waves at least up to 100 s: it has been shown (Montagner and Jobert, 1988) that standard perturbation theory is inadequate to correct for crustal correction and more rigorous approaches have been proposed (Li and Romanowicz, 1996; Boschi and Ekström, 2002; Zhou *et al.*, 2005) using the updated crustal models 3SMAC (Nataf and Ricard, 1996; Ricard *et al.*, 1996) or CRUST2.0 (Mooney *et al.*, 1998; Laske *et al.*, 2001).

As an example of the results obtained after the first step of the tomographic procedure, **Figure 4** shows different maps of 2-Ψ azimuthal anisotropy for Rayleigh waves at 100 s period for the first three modes, $n = 0,1,2$, superimposed on the isotropic part (0-Ψ term) of phase velocity (Beucler and Montagner, 2006). From petrological and mineralogical considerations, Montagner and Nataf (1988) and Montagner and Anderson (1989a, 1989b) showed that the predominant terms of phase velocity azimuthal expansion are the 0-Ψ and 2-Ψ for Rayleigh waves, and 0-Ψ and 4-Ψ for Love waves. However, Trampert and Woodhouse (2003) carefully addressed the requirement of azimuthal anisotropy, and demonstrated that Rayleigh wave data need both 2-Ψ and 4-Ψ terms, which is also confirmed by Beucler and Montagner (2006). It was shown that for the same variance reduction, a global parametrization of anisotropy including azimuthal anisotropy requires fewer parameters than an isotropic parametrization. This apparent paradox can be explained by the fact that the increase of physical parameters is largely compensated by the smaller number of geographical

Author's personal copy

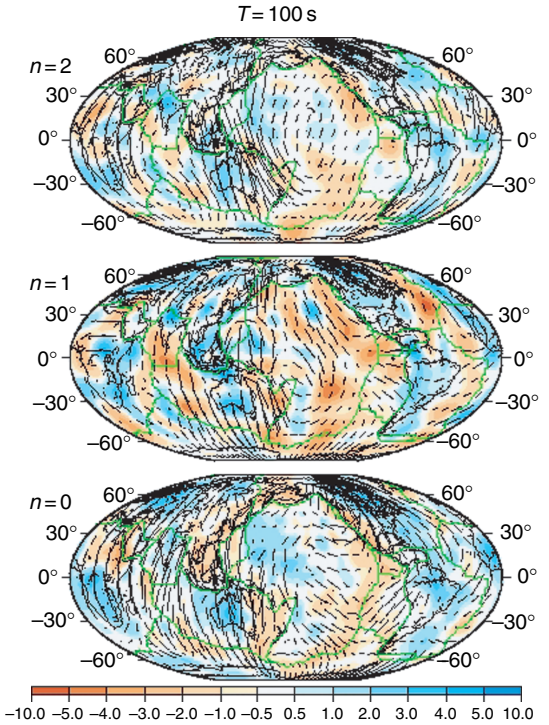


Figure 4 Rayleigh wave phase velocity maps at period $T = 100$ s for the first three modes ($n = 0, 1, 2$). Modified from Beucler E and Montagner J-P (2006) Computation of large anisotropic seismic heterogeneities. *Geophysical Journal International* 165: 447–468.

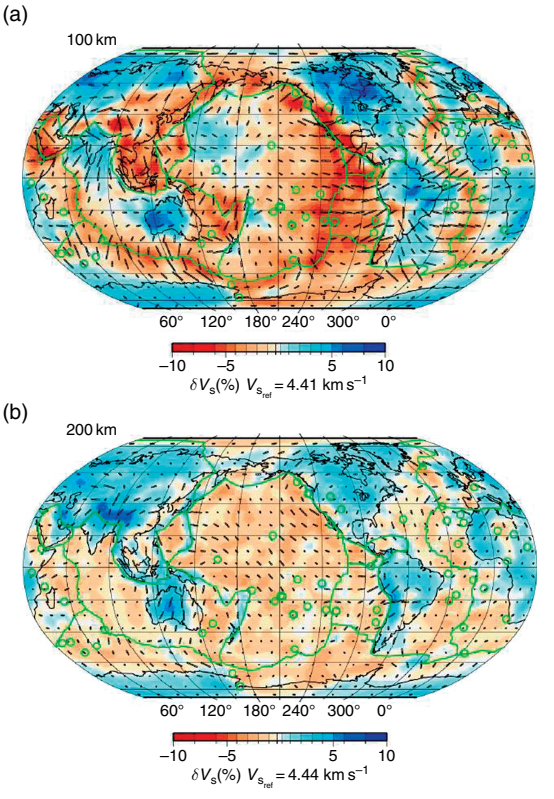


Figure 5 (a, b) Two cross-sections at 100 km (top) and 200 km (bottom) depths of the global tomographic model of Debayle *et al*. (2005). Directions of azimuthal anisotropy are superimposed on S-wave velocity heterogeneities. The length of bars is proportional to its amplitude (<2%).

parameters, that is, larger-scale heterogeneities. Other tests have questioned whether phase data are sensitive enough to detect azimuthal anisotropy (Larson *et al*., 1998; Laske and Masters 1998) and the use of additional polarization data has been proposed.

Most tomographic models agree that down to ~250–300 km, the deep structure is closely related to plate tectonics and continental distribution. **Figure 5** presents two horizontal cross-sections from the most recent model of Debayle *et al*. (2005), which illustrates and confirms the robust features of the upper mantle models published so far since Montagner and Tanimoto (1991). In the upper mantle depth range around 100 km, all plate boundaries are slow: ridges and back-arc areas are slow, shields are fast, and seismic velocity in oceanic areas is increasing with the age of the seafloor. Except at few places, it is found that radial anisotropy expressed through the ξ parameter ($\xi = (V_{SH}^2 - V_{SV}^2)/V_{SV}^2$) is positive, as large as 10% in some oceanic areas and decreases with depth.

The amplitude of SV-wave azimuthal anisotropy (G parameter) presents an average value of ~2% below oceanic areas (**Figure 5**). Montagner (1994, 2002) noted a good correlation between seismic azimuthal anisotropy and plate velocity directions (primarily for fast moving plates) given by Minster and Jordan (1978) or DeMets *et al*. (1990). However, the azimuth of G parameter can vary significantly as a function of depth. For instance, at shallow depths (down to 60 km), the maximum velocity can be parallel to mountain belts or plate boundaries (Vinnik *et al*., 1992; Silver, 1996; Babuska *et al*., 1998), but orthogonal to them at large depth. This means that, at a given place, the orientation of fast axis is a function of depth, which explains why the interpretation of SKS splitting with a simple model is often difficult.

As depth increases, the amplitude of heterogeneities rapidly decreases, some trends tend to vanish, and some distinctive features come up: most fast

Author's personal copy

ridges are still slow but slow ridges are hardly visible and back-arc regions are no longer systematically slow below 200 km. Large portions of fast ridges are offset with respect to their surface signatures. Below 300 km of depth (not shown here), high-velocity body below the western and the eastern Pacific rim is the most striking feature, which can be related to subducting slabs.

A visual and quantitative comparison of existing models can be found in the reference Earth model (REM) web site.

1.16.4 Geodynamic Applications

The most popular application of large-scale tomographic models is the understanding of mantle convection. Seismic velocity anomalies can be converted, under some assumptions, into temperature anomalies, density anomalies, and also into chemical or mineralogical heterogeneities. The application of seismic anisotropy to geodynamics in the upper mantle is straightforward if we assume that, due to the lattice-preferred orientation (LPO) of anisotropic crystals such as olivine (Christensen and Lundquist, 1982; Nicolas *et al.*, 1973), the fast-polarization axis of mineralogical assemblages is in the flow plane parallel to the direction of flow. **Figure 6** shows what is expected for the observable parameters V_S, ξ, G, ψ_G in the case of a simple convective cell with LPO. Radial anisotropy ξ expresses the vertical ($\xi < 1$) or horizontal character ($\xi > 1$) of convective flow, and the azimuthal anisotropy **G** can be related to the horizontal flow direction. Conversely, the three maps of V_S, ξ, **G**, can be interpreted in terms of convective flow. These three pieces of information are necessary to correctly interpret the data. For example, upwellings or downwellings are both characterized by a weak or negative ξ parameter, but a correlative positive or negative δV_S discriminates between these possibilities. By simultaneously inverting at depth for the different azimuthal terms of Rayleigh and Love waves, it is therefore possible to separate the lateral variations in temperature from those induced by the orientation of minerals. Such an interpretation might, however, be erroneous in water-rich mantle regions where LPO of minerals such as olivine is not simply related to the strain field (e.g., Jung and Karato, 2001). We will only present some examples of interesting applications of anisotropy in large-scale geodynamics and tectonics.

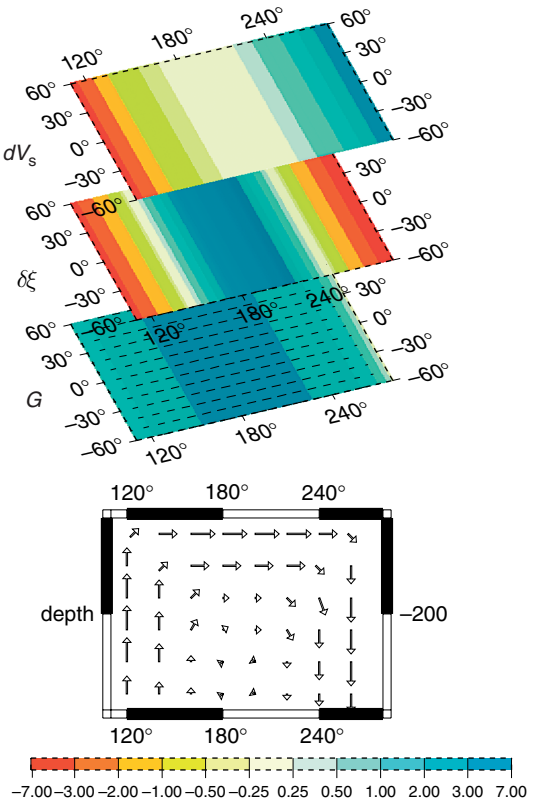


Figure 6 Horizontal cross sections of the seismic observable parameters V_s, ξ, G, Ψ_G associated with a simple convecting cell in the upper mantle, assuming LPO of anisotropic minerals such as olivine. A vertical flow is characterized by a negative ξ radial anisotropy (ratio between V_{SH} and V_{SV}, and a small azimuthal anisotropy ($G \approx 0$). An upwelling (resp. downwelling) is characterized by a large positive (resp. negative) temperature anomaly inducing $\delta V_s < 0$ (resp. $\delta V_s > 0$). A predominant large-scale horizontal flow will be translated into a significant amplitude of the G azimuthal anisotropy and its orientation will reflect the direction of flow (with a 180° ambiguity). Modified from Montagner J-P (2002) Upper mantle low anisotropy channels below the Pacific plate. *Earth and Planetary Science Letters* 202: 205–227.

Seismic anisotropy in the mantle primarily reflects the strain field prevailing in the past (frozen-in anisotropy) for shallow layers or present convective processes in deeper layers. Therefore, it makes it possible to map convection in the mantle. It must be noted that, when only the radial anisotropy is retrieved, its interpretation is nonunique. A fine layering of the mantle can also generate such a kind of anisotropy, and neglecting the azimuthal anisotropy can bias the amplitude of radial anisotropy and its interpretation.

Author's personal copy

The uppermost mantle down to 410 km is the depth range where the existence of seismic anisotropy is now widely recognized and well documented. Azimuthal variations have been found for body waves and surface waves in different areas of the world. During the last years, the shear wave splitting, primarily for SKS waves has extensively been used to study continental deformation, but very few studies using body waves are devoted to oceanic areas. Conversely, global anisotropic upper mantle models have been primarily derived during the last 10 years from surface waves, which are sensitive to structure below oceanic areas in the absence of ocean bottom stations and consequently of dense body wave data. The intercomparison of anisotropic body wave and surface wave data is still in its infancy. However, as shown by Montagner *et al.* (2000), Vinnik *et al.* (2003), and Simons *et al.* (2002), such a comparison is providing encouraging results.

1.16.4.1 Oceanic Plates

Oceans are the areas where plate tectonics applies almost perfectly and this is particularly the case in the largest one, the Pacific plate. **Figure 7** presents three vertical cross-sections at two different latitudes, displaying V_{SV} velocity anomalies (**Figure 7**(**a**)) and the two kinds of anisotropy, which can be retrieved by simultaneous inversion of Rayleigh and Love waves constant 0-Ψ and azimuthal terms of eqn (1) from the model of Montagner (2002). In **Figure 7**(**b**), the equivalent radial anisotropy of the medium, for S-wave expressed through the ξ parameter, is displayed. The maps of **Figure 7**(**c**) are the distributions of the G parameter related to the azimuthal variation of SV-wave velocity. The maximum amplitude of G is $\sim$5% and rapidly decreases as depth increases. The distributions of velocity and anisotropy are completely different for these different cross-sections. The thickening of lithosphere with the age of the seafloor is well observed on V_{SV} velocity maps, but lithosphere is much thicker in the northern cross-section. When compared with the cooling half-space model, bathymetry, heat flux and lithospheric thickness flatten with age (see Ritzwoller *et al.* (2004) for recent results). This flattening is explained by basal reheating, especially in the Central Pacific and the birth of small-scale convection below the lithosphere (Davaille and Jaupart, 1994; Solomatov and Moresi, 2000).

Radial cross-sections (**Figure 7**(**b**)) show that the $\delta\xi = \xi - \xi_{PREM}$ parameter is usually negative and small, where flow is primarily radial (mid-ocean ridges and subduction zones). For the East-Pacific Rise, Gu *et al.* (2005) found that a negative radial anisotropy is observed at least down to 300 km. Between plate boundaries, oceans display very large areas with a large positive radial anisotropy such as in the Pacific Ocean (Ekström and Dziewonski, 1998), characteristic of an overall horizontal flow field. This very large anisotropy in the asthenosphere might be the indication of a strong deformation field at the base of the lithosphere (Gung *et al.*, 2003), corresponding to the upper boundary layer of the convecting mantle (Anderson and Regan, 1983; Montagner, 1998).

Since convective flow below oceans is dominated by large-scale plate motions, the long-wavelength anisotropy found in oceanic lithospheric plates and in the underlying asthenosphere should be similar to the high-resolution anisotropy measured from body waves. Incidentally, one of the first evidences of azimuthal anisotropy was found in the Pacific Ocean by Hess (1964) for Pn-waves. So far, there are very few measurements of anisotropy by SKS splitting in the oceans. Due to the lack of seismic stations on the sea floor (with the exception of H2O half-way between Hawaii and California), the only measurements available for SKS were performed in stations located on ocean islands (Ansel and Nataf, 1989; Kuo and Forsyth, 1992; Russo and Okal, 1999; Wolfe and Silver, 1998), which are by nature anomalous objects, such as volcanic hotspots, where the strain field is perturbed by the upwelling material and not necessarily representative of the main mantle flow field. SKS splitting was measured during the temporary MELT experiment on the East-Pacific Rise (Wolfe and Solomon, 1998) but the orientation of the splitting is in disagreement with the petrological predictions of Blackman *et al.* (1996). Walker *et al.* (2001) presented a first measurement of SKS splitting at H2O, but it is in disagreement with independent SKS splitting measurements at the same station by Vinnik *et al.* (2003) and with surface wave anisotropy (Montagner, 2002).

The large-scale azimuthal anisotropy within and below lithosphere in the depth range 100–300 km is closely related to plate motions (Montagner, 1994; Ekström, 2000) and modeled in this framework (Tommasi *et al.*, 1996). Fast-moving oceanic plates are zones where the comparison between directions of plate velocities (Minster and Jordan, 1978) or

Author's personal copy

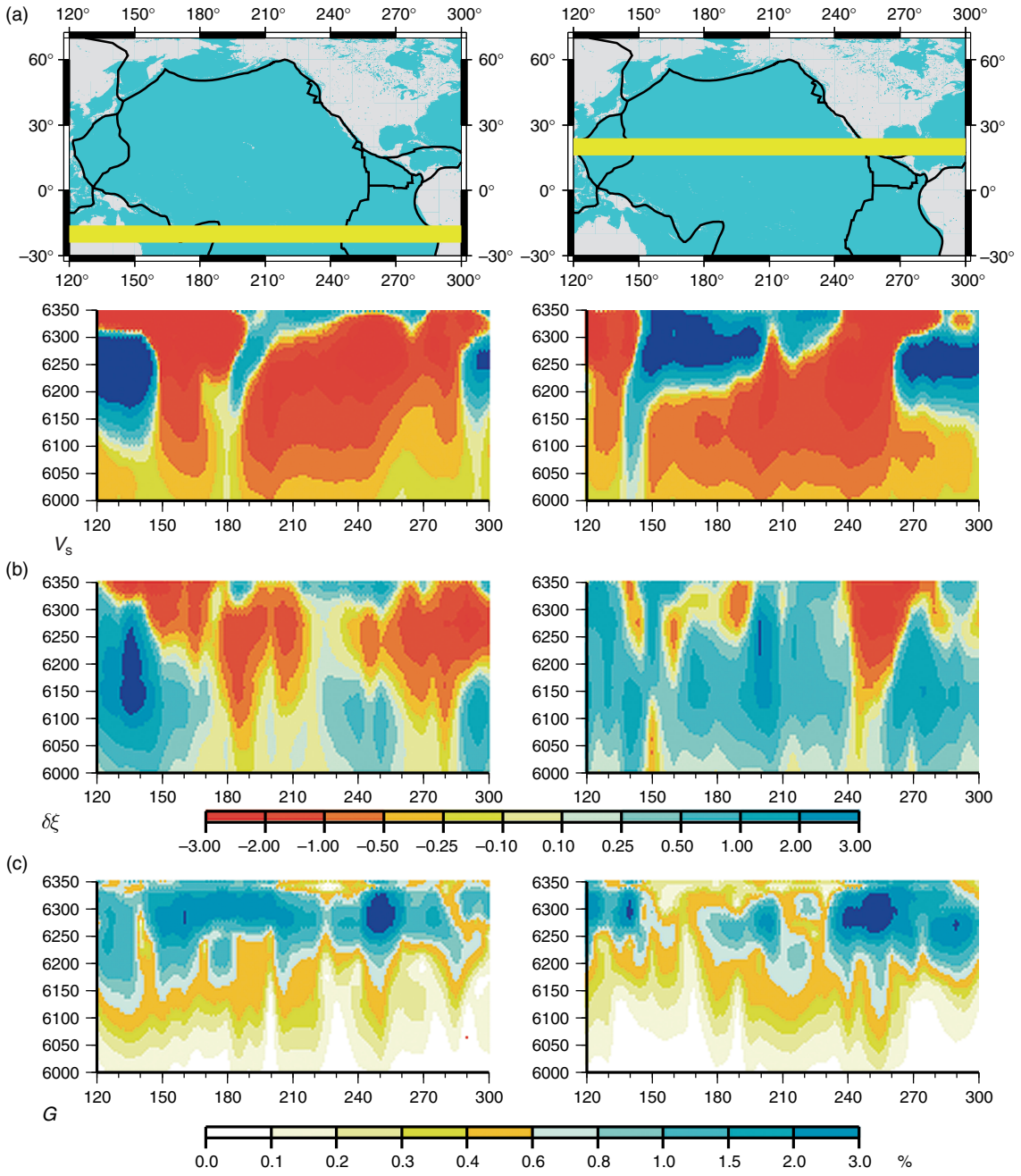


Figure 7 Vertical cross-sections of the distribution of V_s, $\xi - \xi_0$, G in the Pacific plate at $-20°$ south and $20°$ north between radii 6000 km (370 km depth) and 6350 km (20 km depth) (after Montagner, 2002). The color scales in percents are the same for V_s and ξ. The vertical scale is exaggerated to make the figures more readible. (a) V_s; (b) $\delta\xi = \xi - \xi_0$: deviation of ξ with respect to a reference model (ξ_0 PREM model); (c) G: amplitude of azimuthal anisotropy parameters.

NUVEL-1 (DeMets *et al.*, 1990) and directions of G parameter is the most successful (**Figure 8**). Conversely, such a comparison is more difficult and controversial below plates bearing a large proportion of continents, such as the European–Asian plate, characterized by a very small absolute motion in the hotspot reference frame and probably a large influence of inherited anisotropy.

The map with the G parameter at 100 km (**Figure 5**) as well as the cross-sections of **Figure 7**(**c**)

Author's personal copy

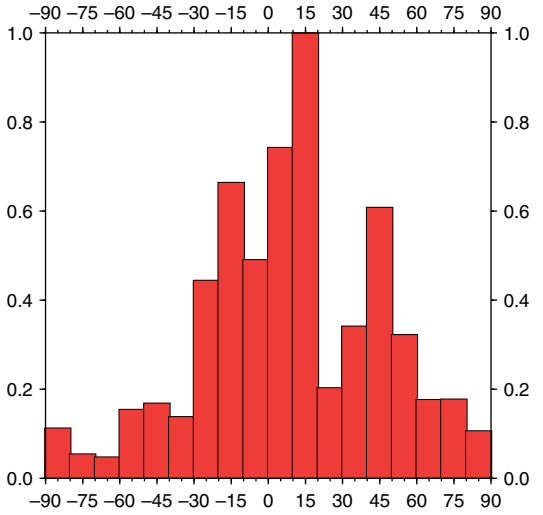


Figure 8 Histogram of the difference between plate velocities directions and synthetic SKS anisotropy azimuths in the Pacific plate. It is calculated by summing the contributions of each grid point (5°×5°) weighted by the latitude and the amplitude of anisotropy. Modified from Montagner J-P (2002) Upper mantle low anisotropy channels below the Pacific plate. *Earth and Planetary Science Letters* 202: 205–227.

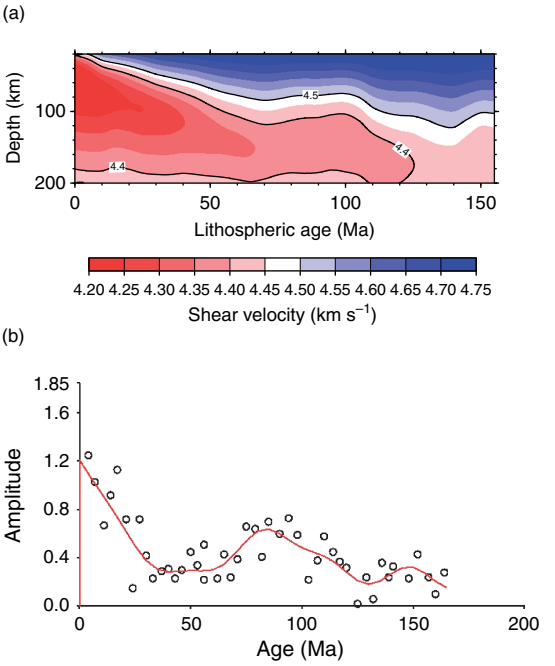


Figure 9 Variations of (a) average S-wave velocity and (b) azimuthal anisotropy (through the delay time of synthetic SKS splitting) plotted versus the age of lithosphericsea floor. In both cases the structure below the plate for age between 60 and 100 Ma looks anomalous. (a) Modified from Ritzwoller MH, Shapiro NM, and Zhong S-J (2004) Cooling history of the Pacific lithosphere. *Earth and Planetary Science Letters* 226: 69–84. (b) After Montagner J-P (2002) upper mantle low anisotropy channels below the Pacific plate. *Earth and Planetary Science Letters* 202: 205–227.

show that the azimuthal anisotropy is very large along spreading ridges with a large asymmetry for the East-Pacific Rise. The direction of anisotropy is in very good agreement with plate motion, which is also found in all other available models (Ekström, 2000; Smith *et al.*, 2004; Debayle *et al.*, 2005). The anisotropy is also large in the middle of the Pacific plate, but a line of very small azimuthal anisotropy almost parallel to the East-Pacific Rise is observed there (see also **Figure 2** for synthetic SKS). This linear area of small anisotropy was named low anisotropy channel (LAC) by Montagner (2002). When calculating the variation of the amplitude of azimuthal anisotropy as a function of depth, a minimum comes up between 40 and 60 Ma age of the seafloor (**Figure 9**(**a**)). The LAC is presumably related either to cracking within the Pacific plate and/or to secondary convection within and below the rigid lithosphere, predicted by numerical and analog experiments and also translated in the V_S velocity structure (Ritzwoller *et al.*, 2004; **Figure 9**(**b**)). These new features provide strong constraints on the decoupling between the plate and asthenosphere. The existence and location of these LACs might be related to the current active volcanoes and hotspots (possibly plumes) in Central Pacific. LACs, which are dividing the Pacific plate into smaller units, might indicate a future reorganization of plates with ridge migrations in the Pacific Ocean. They call for more thorough numerical modeling.

1.16.4.2 Continents

Differences in the thickness of high-velocity layer underlying continents as imaged by seismic tomography have fuelled a long debate on the origin of continental roots (Jordan, 1975, 1978). Some global tomographic models provide a continental thickness of ~200–250 km in agreement with heat-flow analysis or electrical conductivity, but others suggest thicker zones up to 400 km.

Seismic anisotropy can provide fundamental information on the structure of continents, their root, and the geodynamic processes involved in mountain building and collision between continents (Vinnik *et al.*, 1992; Silver, 1996) such as in Central Asia (Griot *et al.*, 1998a, 1998b). Radial anisotropy ξ is

Author's personal copy

usually very heterogeneous below continents in the first 150–200 km of depth with positive or negative areas according to geology. But it seems to display a systematic tendency of being positive at larger depth (down to 300 km), whereas it is very large in the oceanic lithosphere in the depth range 50–200 km and decreases rapidly at larger depths (Montagner, 1994). Conversely, radial anisotropy displays a maximum (though smaller than in oceanic lithosphere) below very old continents (such as Siberian and Canadian Shield) in the depth range 200–400 km (Montagner and Tanimoto, 1991). Seismic anisotropy below continents, sometimes confined to the upper 220 km (Gaherty and Jordan, 1995) can still be significant below. A more quantitative comparison of radial anisotropy between different continental provinces is presented in Babuska *et al.* (1998), and demonstrates systematic differences according to the tectonic context. The existence of positive large-scale radial anisotropy below continents at depth might be a good indicator of the continental root which was largely debated since the presentation of the model of tectosphere by Jordan (1975, 1978, 1981). If this maximum of anisotropy is assumed to be related to an intense strain field in this depth range, it might be characteristic of the boundary between continental lithosphere and 'normal' upper mantle material. Gung *et al.* (2003) showed that it is possible to reconcile different isotropic tomographic models by taking into account seismic anisotropy. They find that significant radial anisotropy (with $V_{SH} > V_{SV}$) under most cratons in the depth range 250–400 km, similar to that found at shallower depths (80–250 km) below oceanic basins. Such a result is also in agreement for the Australian continent (Debayle and Kennett, 2000; Simons *et al.*, 2002). So, all results seem to show that the root of continents as defined by radial anisotropy is located between 200 and 300 km. However, this result is not correlated with a maximum in azimuthal anisotropy in this depth range (Debayle and Kennett, 2005): the fast-moving Australian plate seems to be the only continental region with a sufficiently large deformation at its base to be transformed into azimuthal anisotropy. They propose that, for continents other than Australia, weak influence of basal drag on the lithosphere may explain why azimuthal anisotropy is observed only in a layer located in the uppermost 100 km of the mantle. This layer shows a complex organization of azimuthal anisotropy suggesting a frozen-in origin of deformation, compatible with SKS splitting.

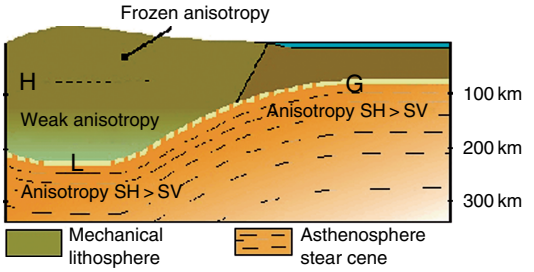


Figure 10 Scheme illustrating the difference in the location of maximum anisotropy between oceans and continents. Modified from Gung Y, Panning M, and Romanowicz B (2003) Global anisotropy and the thickness of continents. *Nature* 422: 707–711.

The difference in radial and azimuthal anisotropies between oceans and continents might reflect a difference of coupling between lithosphere and asthenosphere, through the basal drag. The coupling might be weak below most continental roots, in contrast with the Pacific plate, where the coupling (reflected by plate direction) is the first-order effect in the uppermost 200 km for young ages, before thermal instabilities take place at the base of the lithosphere, as evidenced by the existence of low-anisotropy channels. These results on the difference between oceanic and continental anisotropies are illustrated in **Figure 10**.

1.16.4.3 Velocity and Anisotropy in the Transition Zone

The transition zone plays a key role in mantle dynamics, particularly the 660 km discontinuity, which might inhibit the passage of matter between the upper and the lower mantle. Its seismic investigation is made difficult on the global scale by the poor sensitivity of fundamental surface waves in this depth range and by the fact that teleseismic body waves recorded at continental stations from earthquakes primarily occurring along plate boundaries have their turning point below the transition zone. For body waves, many different techniques using SS precursors (Shearer, 1991) or P-to-S converted waves (Chevrot *et al.*, 1999) were used at global scale to investigate the thickness of the transition zone. In spite of some initial controversies, a recent model by Lawrence and Shearer (2006) provides a coherent large-scale image of the transition zone thickness.

Whatever the type of data (normal mode, higher modes of surface waves, or body waves), an important feature of the transition zone is that, contrarily to the

Author's personal copy

rest of the upper mantle, the upper transition zone is characterized by a large degree-2 pattern (Masters *et al.*, 1982), and to a less extent, a strong degree-6. The degree-2 pattern (as well as degree-6) can be explained by the predominance of a simple large-scale flow pattern characterized by two upwellings in central Pacific Ocean and Eastern Africa and two downwellings in the Western and Eastern Pacific Ocean (Montagner and Romanowicz, 1993), proposed initially in the lower mantle (Busse, 1983). This scheme was corroborated by the existence, in the upper transition zone, of a slight but significant degree-4 radial anisotropy displayed by Montagner and Tanimoto (1991) and Roult *et al.* (1990) in agreement with the prediction of this model. Therefore, the observations of the geographical distributions of degrees 2, 4, 6 in the transition zone are coherent and spatially dependent. Montagner (1994) compared these different degrees to the corresponding degrees of the hotspot and slab distribution. In this simple framework, the distribution of plumes (degree 2+6) are merely a consequence of the large-scale simple flow in the transition zone. The degree 6 of velocity in the transition zone is well correlated with the distribution of hotspots and might indicate that many mantle plumes might originate in the transition zone. Ritsema and van Heijst (2004) observe lower-than-average shear velocity at eight hotspots in this depth range (**Figure 11**). These results suggest that there are different families of plumes, some of them originating in the transition zone.

As for anisotropy in the transition zone, Montagner and Kennett (1996), by using eigenfrequency data, display some evidence of radial anisotropy in the upper (410–660 km) and lower (660–900 km) transition zones. Gung *et al.* (2003) also display a slight maximum of the degree-0 ξ in the transition zone. The existence of anisotropy close to the 660 km discontinuity was also found by Vinnik and Montagner (1996) below Germany, and by Vinnik *et al.* (1998) in Central Africa. By studying P-to-S converted waves at the GRF network and at GEOSCOPE station BNG in Central Africa, they observed that part of the initial P-wave is converted into SH wave. This signal can be observed on the transverse component of seismograms. The amplitude of this SH wave cannot be explained by a dipping 660 km discontinuity and it constitutes a good evidence for the existence of anisotropy just above this discontinuity. However, there is some evidence of lateral variation of anisotropy in the transition zone as found by the investigation of several subduction zones (Fischer and Yang, 1994; Fischer and Wiens, 1996). Fouch and Fischer (1996) present a synthesis of these different studies and show that some subduction zones such as Sakhalin Islands require deep anisotropy in the transition zone, whereas others, such as Tonga, do not need any anisotropy. They conclude that their data might be reconciled by considering the upper transition zone (410–520 km) intermittently anisotropic, and the rest of the transition zone might be isotropic.

Anisotropy in the transition zone was also advocated by two independent studies, using different data sets. The observations of Wookey *et al.* (2002), though controversial, present evidence of very large S-wave splitting (up to 7 s) in the vicinity of the 660 km discontinuity between Tonga–Kermadec subduction zone and Australia. On a global scale, Trampert and van Heijst (2002) show a long-wavelength azimuthal anisotropic structure in the transition zone. The root-mean-square amplitude of lateral variations of G is ~1%. Beghein and Trampert (2003), using probability density functions and separating ξ, ϕ, and η anisotropies, suggest a chemical component to explain these different parameters. The interpretation of these new tentative results is not obvious and new data are necessary to close the debate on the nature of velocity and anisotropy heterogeneities in the transition zone. The transition zone might be a mid-mantle boundary layer, and a detailed and reliable tomographic model of S-wave velocity and anisotropy in the transition zone will provide fundamental insights into the dynamic of the whole mantle.

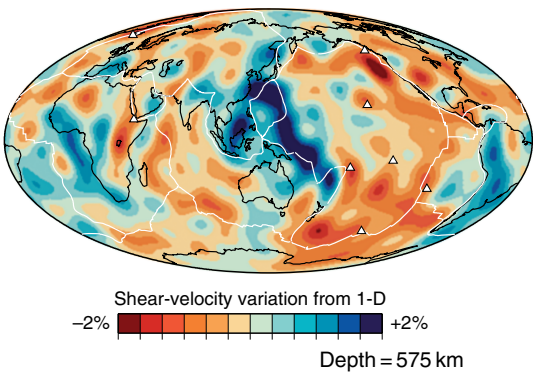


Figure 11 Shear-velocity variation and hotspot distribution. Modified from Ritsema J and van Heijst HJ (2004) Global transition zone tomography. *Journal of Geophysical Research* 109: B02302 doi:10.1029/2003JB002610.

Author's personal copy

1.16.5 Numerical Modeling and Perspectives

In the previous sections, we have highlighted the presence of lateral heterogeneities in seismic velocity and anisotropy in different parts of the Earth's upper mantle. However, anisotropy is not present in all depth ranges nor at all scales. There is some consensus for the presence of radial anisotropy in many parts of the upper mantle in order to simultaneously explain Love-wave and Rayleigh-wave dispersion, and even in the lower mantle (Panning and Romanowicz , 2004). The existence of azimuthal anisotropy is more controversial, though, from petrological reasons, it turns out that radial anisotropy and azimuthal anisotropy are intimately related and should be searched for simultaneosuly. Additional data, such as polarization data, might help to provide additional constraints on both kinds of anisotropy (Yu and Park, 1993; Pettersen and Maupin, 2002). But it requires the development of improved theoretical and numerical methods in order to work on the amplitude of seismograms.

Thanks to the access to very powerful computers, we are at the beginning stage of a new era for seismology. The twentieth century was dominated by the use of ray theory, and later on the normal mode theory. Since it is now feasible to numerically compute synthetic seismograms in complex 3-D structures in global spherical geometry (Komatitsch and Vilotte, 1998; Komatitsch and Tromp, 1999; Capdeville *et al.*, 2003), it is possible to model the complex interaction between seismic waves and 3-D heterogeneity, particularly in anisotropic, anelastic media. Some new and sophisticated tomographic methods are presently developed (Montelli *et al.*, 2004; Capdeville *et al.*, 2005; Tromp *et al.*, 2005; Zhou *et al.*, 2006) that should provide access to the complexity of the Earth mantle by the mapping of short-scale heterogeneities such as mantle plumes, in anisotropic and anelastic media.

A second important challenge is the complete understanding of the origin of anisotropy from the mineral scale up to global scale in the different layers of the Earth. In the upper mantle, seismic anisotropy is due to LPO of anisotropic minerals such as olivine at large scales, requiring several strong conditions, starting with the presence of anisotropic crystals up to the existence of an efficient large scale present or past strain field. In order to fill the gap between grain scale modeling (McKenzie, 1979; Ribe, 1989; Kaminski and Ribe, 2001) and large-scale anisotropy measurements in a convective system (Tommasi *et al.*, 2000), there is now a real need to make more quantitative comparisons between seismic anisotropy and numerical modeling. Gaboret *et al.* (2003) and Becker *et al.* (2003) calculated the convective circulation in the mantle by converting perturbations of S-wave velocity into density perturbations. **Figure 12** shows two cross-sections through the Pacific hemisphere and the associated flow lines (Gaboret *et al.*, 2003) derived from the tomographic model of Ekström and Dziewonski (1998). This kind of modeling makes it possible to calculate the strain tensor and to test different hypotheses for the prevailing mechanisms of alignment, by comparison with seismic data.

The upper mantle is the best known of the deep layers of the earth, where there is now good agreement between many isotropic global tomographic models. But the account of seismic anisotropy is mandatory to avoid biased isotropic heterogeneities. The main application of anisotropy is the mapping of mantle convection and its boundary layers (Karato, 1998; Montagner, 1998). The finding of anisotropy in the transition zone (if confirmed) will provide strong constraints on the flow circulation and the exchange of matter between the upper and the lower mantle. Pursuing the first pionneering efforts, the systematic modeling of the complete seismic waveform in 3-D heterogeneous, anisotropic and anelastic media associated with new techniques of numerical modeling of seismograms will probably enhance our vision of the whole mantle.

In parallel to these theoretical and numerical challenges, there is a crucial need for instrumental developments since there are still many areas at the surface of Earth devoid of broadband seismic stations. These regions are primarily located in Southern Hemisphere and more particularly in oceanic areas where no islands are present. Therefore, an international effort is ongoing, coordinated through International Ocean Network (ION) in order to promote the installation of geophysical ocean bottom observatories in order to fill the enormous gaps in the station coverage (for a description of ION).

Appendix 1: Effect of Anisotropy on Surface Waves in the Plane-Layered Medium

The half-space is assumed to be homogeneous and may be described by its density $\rho(z)$ and its fourth-order elastic tensor $\Gamma(z)$ with 21 independent elastic coefficients. All these parameters are so far supposed independent of x and y coordinates (in **Figure 13**, z is

Author's personal copy

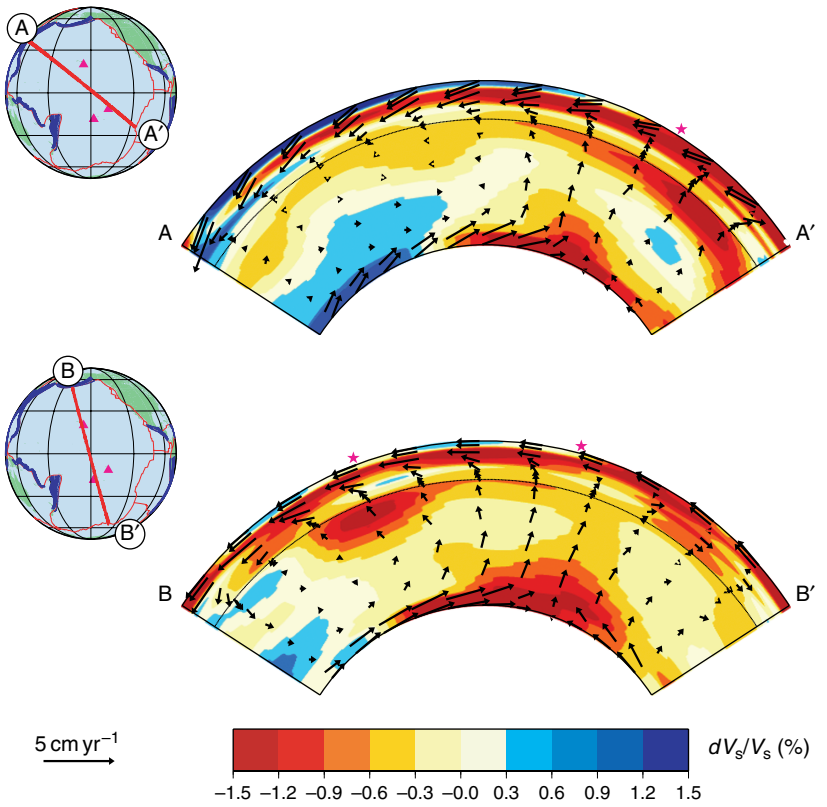


Figure 12 Mantle heterogeneities and convective flow below the Pacific Ocean. Modified from Gaboret C, Forte A, and Montagner J-P (2003) The unique dynamics of the Pacific Hemisphere mantle and its signature on seismic anisotropy. *Earth and Planetary Science Letters* 208: 219–223.

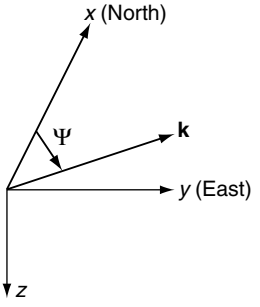


Figure 13 Definition of the Cartesian coordinate system (x, y, z) used in the calculations; Ψ is the azimuth of the wavevector with respect to north.

the vertical component). This condition will be released in the next section. The unperturbed medium is assumed isotropic with an elastic tensor $\Gamma_0(z)$. In that medium, the two cases of Love and Rayleigh wave dispersion can be successively considered.

The unperturbed Love wave displacement is of the form:

$$\mathbf{u}(\mathbf{r},\ t) = \begin{pmatrix} -W(z)\sin\Psi \\ W(z)\cos\Psi \\ 0 \end{pmatrix} \exp(\mathrm{i}[k(x\cos\Psi + y\sin\Psi) - \omega t]) \qquad [19]$$

where $W(z)$ is the scalar depth eigenfunction for Love waves, k is the horizontal wave number, and Ψ is the azimuth of the wave number k measured clockwise from the north.

The unperturbed Rayleigh wave displacement is of the form

$$\mathbf{u}(\mathbf{r},\ t) = \begin{pmatrix} V(z)\cos\Psi \\ V(z)\sin\Psi \\ iU(z) \end{pmatrix} \exp(\mathrm{i}[k(x\cos\Psi + y\sin\Psi) - \omega t]) \qquad [20]$$

where $V(z)$ and $U(z)$ are the scalar depth eigenfunctions for Rayleigh waves. The associated strain tensor $\epsilon(\mathbf{r}, t)$ is defined by

$$\epsilon_{ij}(\mathbf{r},\ t) = 1/2(u_{i,j} + u_{j,i}) \qquad [21]$$

Author's personal copy

where ,*j* denotes the differentiation with respect to the *j*th coordinate. The medium is perturbed from $\Gamma_0(z)$ to $\Gamma_0(z)+\gamma(z)$, where $\gamma(z)$ is small compared to $\Gamma_0(z)$ but quite general in the sense that there is no assumption on the kind of anisotropy. This means that in this approximation we can still consider quasi-Love modes and quasi-Rayleigh modes (Crampin, 1984). From Rayleigh's principle, the first-order perturbation $\delta V(\mathbf{k})$ in phase velocity dispersion is (Smith and Dahlen, 1973, 1975):

$$\delta V(\mathbf{k}) = \frac{V}{2\omega^2}\frac{\int_0^\infty \gamma_{ijkl}\epsilon_{ij}\epsilon^*_{kl}}{\int_0^\infty \rho_0 u_k u^*_k \mathrm{d}z}\mathrm{d}z \qquad [22]$$

where u_i and ϵ_{ij} are, respectively, the displacement and the strain for the unperturbed half-space, and the asterisk denotes complex conjugation. Now because of the symmetry of the tensors $\gamma(z)$ and ϵ, we use the simplified index notation c_{ij} and ϵ_i for the elements γ_{ijkl} and ϵ_{ij}, but the number, n_{ij}, of coefficients γ_{ijkl} for each c_{ij} must be taken into account. The simplified index notation for the elastic tensor γ_{ijkl} is defined in a coordinate system (x_1, x_2, x_3) by

$$\gamma_{ijkl} \rightarrow c_{pq} \begin{cases} \text{if } i=j \Rightarrow & p=i \\ \text{if } k=l \Rightarrow & q=k \\ \text{if } i\neq j \Rightarrow & p=9-i-j \\ \text{if } k\neq l \Rightarrow & q=9-k-l \end{cases} \qquad [23]$$

This kind of transformation enables us to relate the fourth-order tensor γ $(3\times3\times3\times3)$ to a matrix c (6×6). The same simplified index notation can be applied to the components of the strain tensor ε_{ij}, transforming the second-order tensor ϵ (3×3) into a vector with six components. However, it is necessary to be careful, because to a given c_{pq} correspond several γ_{ijkl}, and γ_{ijkl} must be replaced by $n_{pq}c_{pq}$, where n_{pq} is the number of γ_{ijkl} giving the same c_{pq}. Therefore, eqn [22] expressing Rayleigh's principle can be rewritten as

$$\delta V(\mathbf{k}) = \frac{V}{2\omega^2}\frac{\int_0^\infty \sum_{ij} n_{ij}c_{ij}\epsilon_i\epsilon^*_j}{\int_0^\infty \rho_0 u_k u^*_k \mathrm{d}z}\mathrm{d}z \qquad [24]$$

We only detail the calculations for Love waves.

Love Waves

By using previous expressions for $\mathbf{u}(\mathbf{r}, t)$, [19], and $\epsilon_{ij}(\mathbf{r}, t)$, [21], the various expressions of strain are

$$\begin{aligned} \epsilon_1 &= -\mathrm{i}\cos\Psi\sin\Psi kW \\ \epsilon_2 &= \mathrm{i}\cos\Psi\sin\Psi kW \\ \epsilon_3 &= 0 \\ \epsilon_4 &= 1/2\cos\Psi W' \\ \epsilon_5 &= -1/2\sin\Psi W' \\ \epsilon_6 &= 1/2\,(\cos^2\Psi-\sin^2\Psi)kW \end{aligned} \qquad [25]$$

where $W' = \mathrm{d}W/\mathrm{d}r$. In **Table 1**, the different terms $n_{ij}c_{ij}\epsilon_i\epsilon^*_j$ are given. We note that when $c_{ij}\epsilon_i\epsilon^*_j$ is a purely imaginary complex, its contribution to $\delta V(k, \Psi)$ is null. When all the contributions are summed, the different terms $\cos^k\Psi\sin^l\Psi$ are such that $k+l$ is

Table 1 Calculation of the various $c_{ij}\epsilon_i\epsilon_j$ for Love waves, with the simplified index notation ($\alpha=\cos\Psi$; $\beta=\sin\Psi$)

n	ij	$c_{ij}\epsilon_i\epsilon_j$
1	11	$c_{11}\alpha^2\beta^2k^2W^2$
1	22	$c_{22}\alpha^2\beta^2k^2W^2$
1	33	0
2	12	$-c_{12}\alpha^2\beta^2k^2W^2$
2	13	0
2	23	0
2	24	0
4	14	$c_{14}(-\mathrm{i}\alpha^2\beta)\frac{kWW'}{2}$
4	15	$c_{15}(i\alpha^2\beta)\frac{kWW'}{2}$
4	16	$c_{16}(-\alpha\beta)(\alpha^2-\beta^2)\frac{k^2W^2}{2}$
4	24	$c_{24}(-i\alpha^2\beta)\frac{kWW'}{2}$
4	25	$c_{25}(-i\alpha\beta^2)\frac{kWW'}{2}$
4	26	$c_{26}(\alpha\beta)(\alpha^2-\beta^2)\frac{k^2W^2}{2}$
4	34	0
4	35	0
4	36	0
4	44	$c_{44}\alpha^2\frac{W'^2}{4}$
8	45	$c_{45}(-\alpha\beta)\frac{W'^2}{4}$
8	46	$c_{46}(-i\alpha)(\alpha^2-\beta^2)\frac{kWW'}{2}$
4	55	$c_{55}\beta^2\frac{W'^2}{4}$
8	56	$c_{56}(i\beta)(\alpha^2-\beta^2)\frac{kWW'}{2}$
4	66	$c_{66}(\alpha^2-\beta^2)\frac{k^2W^2}{4}$

Author's personal copy

even, which is not surprising in the light of the reciprocity principle. Therefore, each term can be developed as a Fourier series in Ψ with only even terms. Finally, it is found that

$$\begin{aligned}\delta V_{\mathrm{L}}(k,\Psi) = \frac{V}{2\omega^2 L_0}\int_0^\infty \mathrm{d}z\Big\{ & k^2 W^2\left[\frac{1}{8}(c_{11}+c_{22}-2c_{12}+4c_{66})\right] \\ & + W'^2\left[\frac{1}{2}(c_{44}+c_{55})\right] + \cos 2\Psi\, W'^2 \\ & \times\left[\frac{1}{2}(c_{44}-c_{55})\right] - \sin 2\Psi\, W'^2 c_{45} - \cos 4\Psi k^2 W^2 \\ & \times\left[\frac{1}{8}(c_{11}+c_{22}-2c_{12}-4c_{66})\right] + \sin 4\Psi\, k^2 W^2 \\ & \times\left[\frac{1}{2}(c_{26}-c_{16})\right]\Big\} \end{aligned} \quad [26]$$

In the particular case of a transversely isotropic medium with a vertical symmetry axis (also named radial anisotropic medium), we have: $c_{11}=c_{22}=\delta A$, $c_{33}=\delta C$, $c_{12}=\delta(A-2N)$, $c_{13}=c_{23}=\delta F$, $c_{44}=c_{55}=\delta L$, $c_{66}=\delta N$, and $c_{14}=c_{24}=c_{15}=c_{25}=c_{16}=c_{26}=0$. The local azimuthal terms vanish and eqn [26] reduces to

$$\delta V_{\mathrm{L}}(k,\Psi) = \frac{1}{2V_{\mathrm{L}}L_0}\int_0^\infty \left\{ W^2\delta N + \frac{W'^2}{k^2}\delta L\right\}\mathrm{d}z \quad [27]$$

Therefore, the same expressions as in Takeuchi and Saito (1972, p. 268) are found in the case of radial anisotropy. The 0-Ψ term of eqn [26] corresponds to the averaging over azimuth Ψ, which provides the equivalent transversely isotropic model with vertical symmetry axis by setting

$$\begin{aligned}\delta N &= \frac{1}{8}(c_{11}+c_{22}) - \frac{1}{4}c_{12} + \frac{1}{2}c_{66} \\ \delta L &= \frac{1}{2}(c_{44}+c_{55})\end{aligned}$$

If we call C_{ij} the elastic coefficients of the total elastic tensor, we can set

$$\begin{aligned}N &= \rho V_{\mathrm{SH}}^2 = \frac{1}{8}(C_{11}+C_{22}) - \frac{1}{4}C_{12} + \frac{1}{2}C_{66} \\ L &= \rho V_{\mathrm{SV}}^2 = \frac{1}{2}(C_{44}+C_{55})\end{aligned}$$

According to eqn [26], the first-order perturbation in Love wave phase velocity $\delta V_{\mathrm{L}}(k,\Psi)$ can then be expressed as

$$\begin{aligned}\delta V_{\mathrm{L}}(k,\Psi) = \frac{1}{2V_{0_{\mathrm{L}}}(k)}[& L_1(k) + L_2(k)\cos 2\Psi + L_3(k)\sin 2\Psi \\ & + L_4(k)\cos 4\Psi + L_5(k)\sin 4\Psi \end{aligned} \quad [28]$$

where

$$\begin{aligned}L_0(k) &= \int_0^\infty \rho W^2 \mathrm{d}z \\ L_1(k) &= \frac{1}{L_0}\int_0^\infty \left(W^2\delta N + \frac{W'^2}{k^2}\delta L\right)\mathrm{d}z \\ L_2(k) &= \frac{1}{L_0}\int_0^\infty -G_{\mathrm{c}}\left(\frac{W'^2}{k^2}\right)\mathrm{d}z \\ L_3(k) &= \frac{1}{L_0}\int_0^\infty -G_{\mathrm{s}}\left(\frac{W'^2}{k^2}\right)\mathrm{d}z \\ L_4(k) &= \frac{1}{L_0}\int_0^\infty -E_{\mathrm{c}}.W'^2\mathrm{d}z \\ L_5(k) &= \frac{1}{L_0}\int_0^\infty -E_{\mathrm{s}}.W'^2\mathrm{d}z\end{aligned}$$

Rayleigh Waves

The same procedure holds for the local Rayleigh wave phase velocity perturbation δV_{R}, starting from the displacement given previously (Montagner and Nataf, 1986):

$$\begin{aligned}\delta V_{\mathrm{R}}(k,\Psi) = \frac{1}{2V_{0_{\mathrm{R}}}(k)}[& R_1(k) + R_2(k)\cos 2\Psi \\ & + R_3(k)\sin 2\Psi + R_4(k)\cos 4\Psi \\ & + R_5(k)\sin 4\Psi \end{aligned} \quad [29]$$

where

$$\begin{aligned}R_0(k) &= \int_0^\infty \rho(U^2+V^2)\mathrm{d}z \\ R_1(k) &= \frac{1}{R_0}\int_0^\infty \left[V^2\delta A + \frac{U'^2}{k^2}\delta C + \frac{2U'V}{k}.\delta F \right. \\ &\quad \left. + \left(\frac{V'}{k}-U\right)^2\delta L\right]\mathrm{d}z \\ R_2(k) &= \frac{1}{R_0}\int_0^\infty \left[V^2 B_c + \frac{2U'V}{k}H_{\mathrm{c}} + \left(\frac{V'}{k}-U\right)^2 G_{\mathrm{c}}\right]\mathrm{d}z \\ R_3(k) &= \frac{1}{R_0}\int_0^\infty \left[V^2 B_s + \frac{2U'V}{k}H_{\mathrm{s}} + \left(\frac{V'}{k}-U\right)^2 G_{\mathrm{s}}\right]\mathrm{d}z \\ R_4(k) &= \frac{1}{R_0}\int_0^\infty E_{\mathrm{c}}V^2\mathrm{d}z \\ R_5(k) &= \frac{1}{R_0}\int_0^\infty E_{\mathrm{s}}V^2 dz\end{aligned}$$

The 13 depth-dependent parameters A, C, F, L, N, B_{c}, B_{s}, H_{c}, H_{s}, G_{c}, G_{s}, E_{c}, and E_{s} are linear combinations of the elastic coefficients C_{ij} and are explicitly given as follows:

- Constant term (0Ψ-azimuthal term: independent of azimuth)

Author's personal copy

$$A = \rho V_{PH}^2 = \frac{3}{8}(C_{11} + C_{22}) + \frac{1}{4}C_{12} + \frac{1}{2}C_{66}$$
$$C = \rho V_{PV}^2 = C_{33}$$
$$F = \frac{1}{2}(C_{13} + C_{23})$$
$$L = \rho V_{SV}^2 = \frac{1}{2}(C_{44} + C_{55})$$
$$N = \rho V_{SH}^2 = \frac{1}{8}(C_{11} + C_{22}) - \frac{1}{4}C_{12} + \frac{1}{2}C_{66}$$

- 2Ψ-azimuthal term

$\cos 2\Psi$	$\sin 2\Psi$
$B_c = \frac{1}{2}(C_{11} - C_{22})$	$B_s = C_{16} + C_{26}$
$G_c = \frac{1}{2}(C_{55} - C_{44})$	$G_s = C_{54}$
$H_c = \frac{1}{2}(C_{13} - C_{23})$	$H_s = C_{36}$

- 4Ψ-azimuthal term

$\cos 4\Psi$	$\sin 4\Psi$
$E_c = \frac{1}{8}(C_{11} + C_{22}) - \frac{1}{4}C_{12} - \frac{1}{2}C_{66}$	$E_s = \frac{1}{2}(C_{16} - C_{26})$

where indices 1 and 2 refer to horizontal coordinates (1: north; 2: east) and index 3 refers to vertical coordinate. ρ is the density, V_{PH}, V_{PV} are, respectively, the horizontal and vertical propagating P-wave velocities, and V_{SH}, V_{SV} the horizontal and vertical polarized S-wave velocities. So, the different parameters present in the different azimuthal terms are simply related to elastic moduli C_{ij}. We must bear in mind that A, C, L, N anisotropic parameters can be retrieved from measurements of the P- and S-wave velocities propagating perpendicular or parallel to the axis of symmetry.

The corresponding kernels are plotted in **Figure 14** for long waves and **Figure 15** for Rayleigh waves.

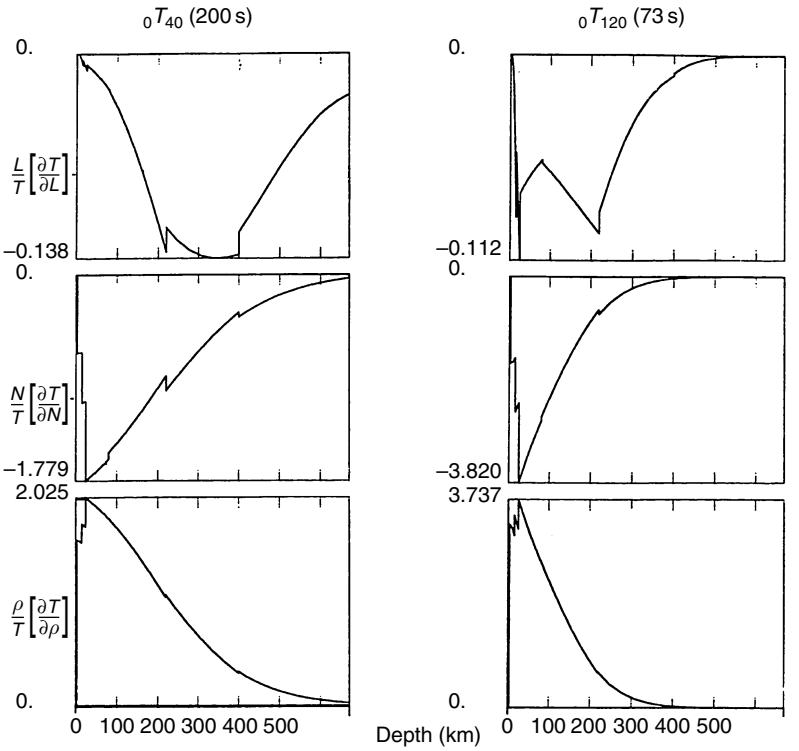


Figure 14 Partial derivatives for Love waves of the period of fundamental normal modes 0T40 (left) and 0T120 (right) with respect to the elastic coefficients of a transversely isotropic Earth, L, N, and density ρ, as a function of depth in the upper mantle (from Montagner and Nataf, 1986). The partial derivatives with respect to A, C, F are null for these modes. The plots are normalized to their maximum amplitudes, given for a $\Delta h = 1000$ km thick perturbed layer. The combinations of elastic coefficients that have the same partial derivative as L are $-G_c$, $-G_s$ for the azimuthal terms 2-Ψ, and as N are E_c, E_s for the azimuthal term 4-Ψ. Note that the amplitude of the L-partial is very small for the fundamental modes, which is not the case for higher modes.

Author's personal copy

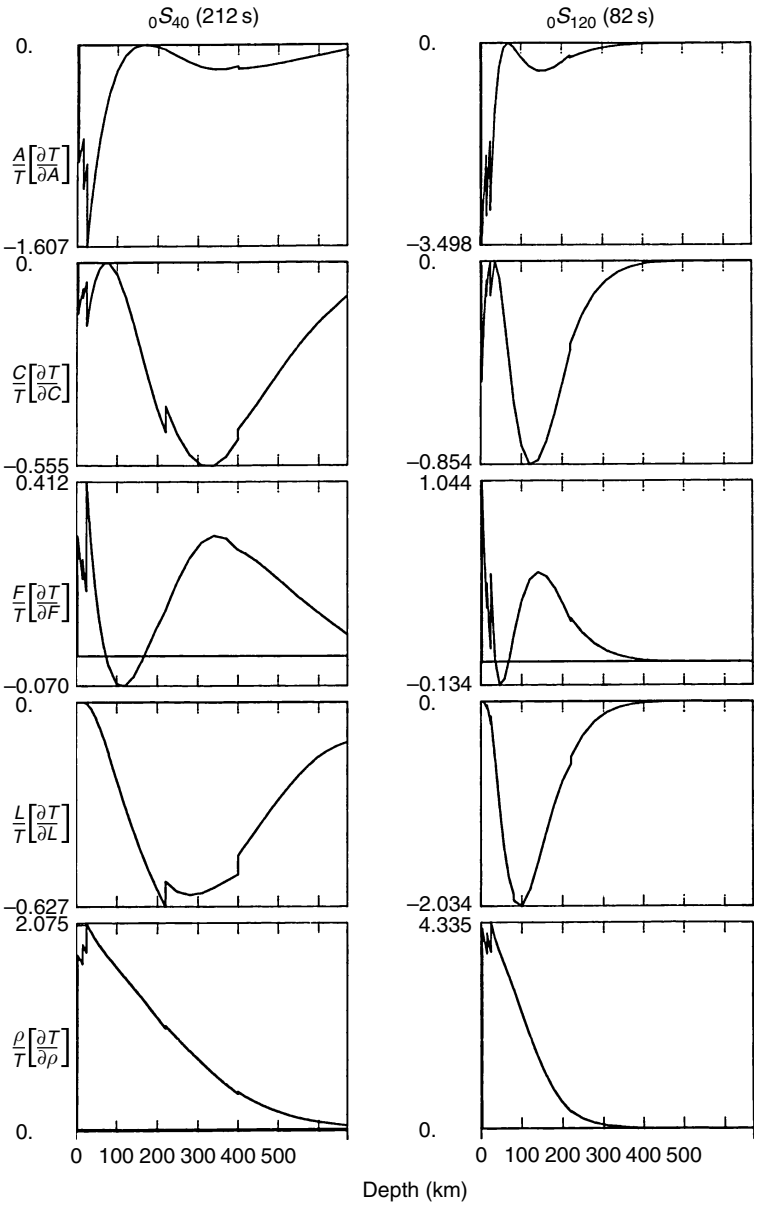


Figure 15 Kernels for Rayleigh waves. Same conventions are applicable as for Figure 13 in the same depth range. The partial derivative with respect to N has not been plotted since its amplitude is very small for fundamental modes. Note that three partials contribute to the 2-Ψ-azimuthal terms, A-partial for B_c, B_s, F-partial for H_c, H_s, and the largest one L-partial for G_c, G_s.

References

Aki K and Richards PG (1980) *Quantitative Seismology: Theory and Methods*. San Fransisco: W. H. Freeman.

Anderson DL (1961) Elastic wave propagation in layered anisotropic media. *Journal of Geophysical Research* 66: 2953–2963.

Anderson DL and Bass JD (1984) Mineralogy and composition of the upper mantle. *Geophysical Research Letters* 11: 637–640.

Anderson DL and Bass JD (1986) Transition region of the Earth's upper mantle. *Nature* 320: 321–328.

Anderson DL and Dziewonski AM (1982) Upper mantle anisotropy: Evidence from fre oscillations. *Geophysical Journal of the Royal Astronomical Society* 69: 383–404.

Anderson DL and Regan J (1983) Upper mantle anisotropy and the oceanic lithosphere. *Geophysical Research Letters* 10: 841–844.

Ansel V and Nataf H-C (1989) Anisotropy beneath 9 stations of the Geoscope broadband network as deduced from shear wave splitting. *Geophysical Research Letters* 16: 409–412.

Babuska V and Cara M (1991) *Seismic Anisotropy in the Earth*. Dordrecht, The Netherlands: Kluwer.

Author's personal copy

Babuska V, Montagner JP, Plomerova J, and Girardin N (1998) Age-dependent large-scale fabric of the mantle lithosphere as derived from surface-wave velocity anisotropy. *Pure and Applied Geophysics* 151: 257–280.

Backus GE and Gilbert F (1967) Numerical applications of a formalism for geophysical inverse problems. *Geophysical Journal of the Royal Astronomical Society* 13: 247–276.

Backus GE and Gilbert F (1968) The resolving power of gross Earth data. *Geophysical Journal of the Royal Astronomical Society* 16: 169–205.

Backus GE and Gilbert F (1970) Uniqueness in the inversion of inaccurate gross Earth data. *Philosophical Transactions of the Royal Society of London Series A* 266: 123–192.

Barmin MP, Levshin AL, and Ritzwoller MH (2001) A fast and reliable method for surface wave tomography. *Pure and Applied Geophysics* 158: 1351–1375.

Bass J and Anderson DL (1984) Composition of the upper mantle: Geophysical tests of two petrological models. *Geophysical Research Letters* 11: 237–240.

Becker TW and Boschi L (2002) A comparison of tomographic and geodynamic mantle models. *Geochemistry Geophysics Geosystems* 3: 2001GC00168.

Becker TW, Kellog JB, Ekström G, and O'Connell RJ (2003) Comparison of azimuthal anisotropy from surface waves and finite-strain from global mantle-circulation models. *Geophysical Journal International* 155: 696–714.

Beghein C and Trampert J (2003) Probability density functions for radial anisotropy: Implications for the upper 1200 km of the mantle. *Earth and Planetary Science Letters* 217: 151–162.

Beucler E and Montagner J-P (2006) Computation of large anisotropic seismic heterogeneities. *Geophysical Journal International* 165: 447–468.

Beucler E, Stutzmann E, and Montagner J-P (2003) Measuring surface wave higher mode velocities by the roller coaster algorithm. *Geophysical Journal International* 155: 289–307.

Blackman DK, Kendall JM, Dawson PR, Wenk HR, Boyce D, and Morgan JP (1996) Teleseismic imaging of subaxial flow at mid-ocean ridges: Traveltime effects of anisotropic mineral texture in the mantle. *Geophysical Journal International* 127: 415–426.

Boschi L and Ekström G (2002) New images of the Earth's upper mantle from measurements of surface wave phase velocity anomalies. *Journal of Geophysical Research* 107: B4 10.1029/2000JB000059.

Busse FH (1983) Quadrupole convection in the lower mantle. *Geophysical Research Letters* 10: 285–288.

Capdeville Y, Chaljub E, Vilotte J-P, and Montagner J-P (2003) Coupling spectral elements and modal solution: A new efficient tool for numerical wave propagation in laterally heterogeneous Earth models. *Geophysical Journal International* 152: 34–66.

Capdeville Y, Gung Y, and Romanowicz B (2005) Towards global earth tomography using the spectral element method: A technique based on source stacking. *Geophysical Journal International* 162: 541–554.

Cara M (1979) Lateral variations of S-velocity in the upper mantle from higher Rayleigh modes. *Geophysical Journal of the Royal Astronomical Society* 57: 649–670.

Cara M and Lévêque J-J (1988) Anisotropy of the asthenosphere: The higher mode data of the Pacific revisited. *Geophysical Research Letters* 15: 205–208.

Chevrot S, Vinnik L, and Montagner J-P (1999) Global-scale analysis of the mantle Pds phase. *Journal of Geophysical Research* 104: 20,203–20,219.

Chevrot S, Favier N, and Komatitsch D (2004) Shear wave splitting in three-dimensional anisotropic media. *Geophysical Journal International* 159: 711–720.

Christensen NI and Lundquist S (1982) Pyroxene orientation within the upper mantle. *Bulletin of the Geological Society of America* 93: 279–288.

Crampin S (1984) An introduction to wave propagation in anisotropic media. *Geophysical Journal of the Royal Astronomical Society* 76: 17–28.

Dahlen FA, Hung S-H, and Nolet G (2000) Fréchet kernels for finite-frequency traveltimes. I: Theory. *Geophysical Journal International* 141: 157–174.

Davaille A and Jaupart C (1994) Onset of thermal convection in fluids with temperature-dependent viscosity: Application to the oceanic mantle. *Journal of Geophysical Research* 99: 19,853–19,866.

Debayle E and Lévêque J-J (1997) Upper mantle heterogeneities in the Indian Ocean from waveform inversion. *Geophysical Research Letters* 24: 245–248.

Debayle E, Cara M, and Lévêque J-J (2001) Seismic evidence for a deeply rooted low velocity anomaly in the upper mantle beneath the northeastern Afro/Arabian continent. *Earth and Planetary Science Letters* 193: 369–382.

Debayle E and Kennett BLN (2000) Anisotropy in the Australasian upper mantle from Love and Rayleigh waveform inversion. *Earth and Planetary Science Letters* 184: 339–351.

Debayle E and Sambridge M (2004) Inversion of massive surface wave data sets: Model construction and resolution assessment. *Journal of Geophysical Research* 109: B02316 doi:10.1029/2003JB002652.

Debayle E, Kennett BLN, and Priestley K (2005) Global azimuthal anisotropy and the unique plate-motion deformation of Australia. *Nature* 433: 509–512.

DeMets C, Gordon RG, Argus DF, and Stein S (1990) Current plate motions. *Geophysical Journal International* 101: 425–478.

Dost B (1990) Upper mantle structure under western Europe from fundamental and higher mode surface waves using the NARS array. *Geophysical Journal of the Royal Astronomical Society* 100: 131–151.

Dziewonski AM (1984) Mapping the lower mantle: Determination of lateral heterogeneity in P velocity up to degree and order 6. *Journal of Geophysical Research* 89: 5929–5952.

Dziewonski AM and Anderson DL (1981) Preliminary reference Earth model. *Physics of the Earth and Planetary Interiors* 25: 297–356.

Dziewonski AM, Chou G, and Woodhouse JH (1981) Determination of earthquake source parameters from waveform modeling. *Journal of Geophysical Research* 86: 2825–2852.

Dziewonski AM and Woodhouse JH (1987) Global images of the Earth's interior. *Science* 236: 37–48.

Ekström G (2000) Mapping the lithosphere and asthenosphere with surface waves: Lateral structure and anisotropy. *AGU monograph,* Eds Richards et al. 121: 239–256.

Ekström G, Tromp J, and Larson EW (1997) Measurements and global models of surface wave propagation. *Journal of Geophysical Research* 102: 8137–8157.

Ekström G and Dziewonski AM (1998) The unique anisotropy of the Pacific upper mantle. *Nature* 394: 168–172.

Fischer KM and Wiens DA (1996) The depth distribution of mantle anisotropy beneath the Tonga subduction zone. *Earth and Planetary Science Letters* 142: 253–260.

Fischer KM and Yang X (1994) Anisotropy in Kuril–Kamtchatka subduction zone structure. *Geophysical Research Letters* 21: 5–8.

Forsyth DW (1975) The early structural evolution and anisotropy of the oceanic upper mantle. *Geophysical Journal of the Royal Astronomical Society* 43: 103–162.

Fouch MJ, Fischer KM, Parmentier EM, Wysession ME, and Clarke TJ (2000) Shear wave splitting, continental keels,

Author's personal copy

patterns of mantle flow. *Journal of Geophysical Research* 105: 6255–6275.
Fouch MJ and Fischer KM (1996) Mantle anisotropy beneath northwest Pacific subduction zones. *Journal of Geophysical Research* 101: 15,987–16,002.
Friederich W (1999) Propagation of seismic shear and surface waves in a laterally heterogeneous mantle by multiple forward scattering. *Geophysical Journal International* 136: 180–204.
Gaboret C, Forte A, and Montagner J-P (2003) The unique dynamics of the Pacific Hemisphere mantle and its signature on seismic anisotropy. *Earth and Planetary Science Letters* 208: 219–233.
Gaherty JB and Jordan TH (1995) Lehmann discontinuity as the base of the anisotropic layer beneath continents. *Science* 268: 1468–1471.
Gilbert F (1971) Excitation of normal modes of the Earth by earthquake sources. *Geophysical Journal of the Royal Astronomical Society* 22: 223–226.
Griot D-A, Montagner JP, and Tapponnier P (1998a) Surface wave phase velocity and azimuthal anisotropy in Central Asia. *Journal of Geophysical Research* 103: 21215–21232.
Griot D-A, Montagner JP, and Tapponnier P (1998b) Heterogeneous versus homogeneous strain in Central Asia. *Geophysical Research Letters* 25: 1447–1450.
Gu YJ, Lerner-Lam A, Dziewonski AM, and Ekström G (2005) Seismic evidence for deep anisotropy beneath the East Pacific Rise. *Earth and Planetary Science Letters* 232: 259–272.
Gung Y, Panning M, and Romanowicz B (2003) Global anisotropy and the thickness of continents. *Nature* 422: 707–711.
Hadiouche O, Jobert N, and Montagner JP (1989) Anisotropy of the African continent inferred from surface waves. *Physics of the Earth and Planetary Interiors* 58: 61–81.
Hess H (1964) Seismic anisotropy of the uppermost mantle under the oceans. *Nature* 203: 629–631.
Ho-Liu P, Montagner J-P, and Kanamori H (1989) Comparison of iterative back-projection inversion and generalized inversion without blocks: Case studies in attenuation tomography. *Geophysical Journal* 97: 19–29.
Jordan TH (1975) The continental tectosphere. *Reviews of Geophysics* 13: 1–12.
Jordan TH (1978) Composition and development of the continental tectosphere. *Nature* 274: 544–548.
Jordan TH (1981) Continents as a chemical boundary layer. *Philosophical Transactions of the Royal Society of London Series A* 301: 359–373.
Jung HY and Karato S-I (2001) Water-induced fabric transitions in olivine. *Science* 293: 1460–1462.
Kaminski E and Ribe NM (2001) A kinematic model for recrystallization and texture development in olivine polycrystals. *Earth and Planetary Science Letters* 189: 253–267.
Karato S-I and Li P (1993) Diffusive creep in perovskite: Implications for the rheology of the lower mantle. *Science* 255: 771–778.
Karato S-I (1998) Seismic anisotropy in the deep mantle, boundary layers and geometry of mantle convection. *Pure and Applied Geophysics* 151: 565–587.
Komatitsch D and Vilotte J-P (1998) The spectral element method: An effective tool to simulate the seismic response of 2D and 3D geological structures. *Bulletin of the Seismological Society of America* 88: 368–392.
Komatitsch D and Tromp J (1999) Introduction of spectral element method for 3-D seismic wave propagation. *Geophysical Journal International* 139: 806–822.
Kuo B-Y and Forsyth DW (1992) A search for split SKS waveforms in North Atlantic. *Geophysical Journal International* 92: 6421–6436.
Larson EWF, Tromp J, and Ekstrom G (1998) Effects of slight anisotropy on surface waves. *Geophysical Journal International* 132: 654–666.
Laske G and Masters G (1998) Surface-wave polarization data and global anisotropic structure. *Geophysical Journal International* 132: 508–520.
Laske G, Masters G, and Reif C (2001) CRUST2.0- a new global crustal model at 2×2 degrees, http://mahi.ucsd.edu/Gabi/crust2.html (2001)
Lawrence JF and Shearer PM (2006) A global study of transition zone thickness using receiver functions. *Journal of Geophysical Research* 111: B06307 doi:10.129/2005JB003973.
Lerner-Lam AL and Jordan TH (1983) Earth structure from fundamental and higher-mode waveform analysis. *Geophysical Journal of the Royal Astronomical Society* 75: 759–797.
Lévêque JJ, Cara M, and Rouland D (1991) Waveform inversion of surface-wave data: A new tool for systematic investigation of upper mantle structures. *Geophysical Journal International* 104: 565–581.
Li X-D and Tanimoto T (1993) Waveforms of long period body waves in a slightly aspherical Earth. *Geophysical Journal International* 112: 92–112.
Li X-D and Romanowicz B (1995) Comparison of global waveform inversions with and without considering cross branch coupling. *Geophysical Journal International* 121: 695–709.
Li X-D and Romanowicz B (1996) Global mantle shear velocity model developed using nonlinear aymptotic coupling theory. *Journal of Geophysical Research* 101: 22245–22273.
Love AEH (1927) *A Treatise on the Theory of Elasticity*, 4th edn., p. 643 Cambridge University Press.
Mainprice DG, Barruol G, and Ben Ismail W (2000) The seismic anisotropy of the Earth's mantle: From single crystal to polycrystal. In, *Earth's deep interior: mineral physics and tomography from the atomic scale to the global scale. Geophysical Monograp* 117: 237.
Marquering H, Snieder R, and Nolet G (1996) Waveform inversions and the significance of surface wave mode coupling. *Geophysical Journal International* 124: 258–278.
Masters G, Jordan TH, Silver PG, and Gilbert F (1982) Aspherical Earth structure from fundamental spheroidal-mode data. *Nature* 298: 609–613.
McKenzie D (1979) Finite deformation during fluid flow. *Geophysical Journal of the Royal Astronomical Society* 58: 687–715.
Minster JB and Jordan TH (1978) Present-day plate motions. *Journal of Geophysical Research* 83: 5331–5354.
Mitchell BJ and Yu G-K (1980) Surface wave dispersion, regionalized velocity models and anisotropy of the Pacific crust and upper mantle. *Geophysical Journal of the Royal Astronomical Society* 63: 497–514.
Mochizuki E (1986) The free oscillations of an anisotropic and heterogeneous Earth. *Geophysical Journal of the Royal Astronomical Society* 86: 167–176.
Mocquet A and Romanowicz B (1989) Three-dimensional structure of the upper mantle beneath the Atlantic Ocean inferred from long-period Rayleigh waves. 2. Inversion. *Journal of Geophysical Research* 95: 6787–6798.
Montagner J-P (1986a) First results on the three dimensional structure of the Indian Ocean inferred from long period surface waves. *Geophysical Research Letters* 13: 315–318.
Montagner J-P (1986b) Regional three-dimensional structures using long-period surface waves. *Annals of Geophysics* 4(B3): 283–294.
Montagner J-P (1994) What can seismology tell us about mantle convection?. *Reviews of Geophysics* 32(2): 115–137.
Montagner J-P (1998) Where can seismic anisotopy be detected in the Earth's mantle? In boundary layers. *Pure and Applied Geophysics* 151: 223–256.

Author's personal copy

Montagner J-P (2002) Upper mantle low anisotropy channels below the Pacific plate. *Earth and Planetary Science Letters* 202: 263–274.

Montagner J-P and Anderson DL (1989a) Constraints on elastic combinations inferred from petrological models. *Physics of the Earth and Planetary Interiors* 54: 82–105.

Montagner J-P and Anderson DL (1989b) Constrained reference mantle model. *Physics of the Earth and Planetary Interiors* 58: 205–227.

Montagner J-P, Griot DA, and Lavé J (2000) How to relate body wave and surface wave anisotropies? *Journal of Geophysical Research* 105: 19,015–19,027.

Montagner J-P and Guillot L (2003) Seismic anisotropy and global geodynamics. *Reviews in Mineralogy and Geochemistry* 51: 353–385.

Montagner J-P and Jobert N (1981) Investigation of upper mantle structure under young regions of the Sout-East Pacific using long-period Rayleigh waves. *Physics of the Earth and Planetary Interiors* 27: 206–222.

Montagner J-P and Jobert N (1988) Vectorial tomography. II: Application to the Indian Ocean. *Geophysical Journal of the Royal Astronomical Society* 94: 309–344.

Montagner J-P and Kennett BLN (1996) How to reconcile body-wave and normal-mode reference Earth models? *Geophysical Journal International* 125: 229–248.

Montagner J-P, Lognonné P, Beauduin R, Roult G, Karczewski J-F, and Stutzmann E (1998) Towards multiscale and multiparameter networks for the next century: The French efforts. *Physics of the Earth and Planetary Interiors* 108: 155–174.

Montagner J-P and Nataf HC (1986) On the inversion of the azimuthal anisotropy of surface waves. *Journal of Geophysical Research* 91: 511–520.

Montagner J-P and Nataf H-C (1988) Vectorial tomography. I: Theory. *Geophysical Journal of the Royal Astronomical Society* 94: 295–307.

Montagner J-P and Tanimoto T (1990) Global anisotropy in the upper mantle inferred from the regionalization of phase velocities. *Journal of Geophysical Research* 95: 4797–4819.

Montagner J-P and Tanimoto T (1991) Global upper mantle tomography of seismic velocities and anisotropies. *Journal of Geophysical Research* 96: 20,337–20,351.

Montagner J-P, Romanowicz B, and Karczewski JF (1994) A first step towards an Oceanic geophysical observatory. *EOS, Transactions of the American Geophysical Union* 75: 150–154.

Montagner J-P and Romanowicz B (1993) Degrees 2, 4, 6 inferred from seismic tomography. *Geophysical Research Letters* 20: 631–634.

Montelli R, Nolet G, Dahlen FA, Masters G, Engdahl R, and Hung S (2004) Finite-frequency tomography reveals a variety of mantle plumes. *Science* 303: 338–343.

Mooney WD, Laske G, and Masters G (1998) CRUST5.1: A global crustal model at 5×5. *Journal of Geophysical Research* 96: 20,337–20,351.

Nataf H-C, Nakanishi I, and Anderson DL (1984) Anisotropy and shear velocity heterogeneities in the upper mantle. *Geophysical Research Letters* 11: 109–112.

Nataf H-C, Nakanishi I, and Anderson DL (1986) Measurement of mantle wave velocities and inversion for lateral heterogeneity and anisotropy, III. Inversion. *Journal of Geophysical Research* 91: 7261–7307.

Nataf H-C and Ricard Y (1996) 3-SMAC: An a priori tomographic model of the upper mantle based on geophysical modeling. *Physics of the Earth and Planetary Interiors* 95: 101–122.

Nicolas A, Boudier F, and Boullier AM (1973) Mechanisms of flow in naturally and experimentally deformed peridototes. *American Journal of Science* 273: 853–876.

Nicolas A and Christensen NI (1987) Formation of anisotropy in upper mantle peridotites: A review. In: Fuchs K and Froidevaux C (eds.) *Composition, Structure and Dynamics of the Lithosphere/ Asthenosphere System*, pp. 111–123. Washington, DC: American Geophysical Union.

Nishimura CE and Forsyth DW (1989) The anisotropic structure of the upper mantle in the Pacific. *Geophysical Journal* 96: 203–229.

Nolet G (1975) Higher Rayleigh modes in Western Europe. *Geophysical Research Letters* 2: 60–62.

Nolet G (1990) Partitioned waveform inversion and two-dimensional structure under the network of autonomously recording seismographs. *Journal of Geophysical Research* 95: 8499–8512.

Okal E and Jo B-G (1985) Stacking investigation of higher-order mantle Rayleigh waves. *Geophysical Research Letters* 12: 421–424.

Panning M and Romanowicz B (2004) Inferences of flow at the base of Earth's mantle based on seismic anisotropy. *Science* 303: 351–353.

Park J and Levin V (2002) Seismic anisotropy: Tracing plate dynamics in the mantle. *Science* 296: 5567.

Pettersen O and Maupin V (2002) Lithospheric anisotropy on the Kerguelen hotspot track inferred from Rayleigh wave polarisation anomalies. *Geophysical Journal International* 149: 225–246.

Plomerova J, Sileny J, and Babuska V (1996) Joint interpretation of upper-mantle anisotropy based on teleseismic P-travel time delay and inversion of shear-wave splitting parameters. *Physics of the Earth and Planetary Interiors* 95: 293–309.

Ribe NM (1989) Seismic anisotropy and mantle flow. *Journal of Geophysical Research* 94: 4213–4223.

Ricard Y, Nataf HC, and Montagner J-P (1996) The 3-SMac model: Confrontation with seismic data. *Journal of Geophysical Research* 101: 8457–8472.

Ringwood AE (1975) *Composition and Petrology of the Earth's Mantle*, 618 pp. New–York: McGraw–Hill.

Ritsema J and van Heijst HJ (2000) Seismic imaging of structural heterogeneity in Earth's mantle: Evidence for large-scale mantle flow. *Science Progress* 83: 243–259.

Ritsema J and van Heijst HJ (2004) Global transition zone tomography. *Journal of Geophysical Research* 109: B02302 doi:10.1029/2003JB002610.

Ritzwoller MH, Shapiro NM, and Zhong S-J (2004) Cooling history of the Pacific lithosphere. *Earth and Planetary Science Letters* 226: 69–84.

Ritzwoller MH, Shapiro NM, Barmin MP, and Levshin AL (2002) Global surface wave tomography. *Journal of Geophysical Research* 107(B12): 2335 10.1029/2002JB001777.

Romanowicz B (1987) Multiplet–multiplet coupling due to lateral heterogeneity: Asymptotic effects on the amplitude and frequency of the Earth's normal modes. *Geophysical Journal of the Royal Astronomical Society* 90: 75–100.

Romanowicz B (1990) The upper mantle degree two: Constraints and inferences from global mantle wave attenuation measurements. *Journal of Geophysical Research* 95: 11051–11071.

Romanowicz B (1995) A global tomographic model of shear attenuation in the upper mantle. *Journal of Geophysical Research* 100: 12375–12394.

Romanowicz B (2002) Inversion of surface waves: A review. In: Lee WHK (ed.) Handbook of Earthquake and Engineering Seismology, ch. 11, pp. 141–173. Amsterdam: Academic Press.

Romanowicz B (2003) Global mantle tomography: Progress status in the past 10 years. *Annual Review of Earth and Planetary Science* 31: 303–328.

Author's personal copy

Romanowicz B, Cara M, Fels J-F, and Rouland D (1984) GEOSCOPE: A French initiative in long period, three component, global seismic networks. *EOS, Transactions of the American Geophysical Union* 65: 753–754.

Romanowicz B and Dziewonski AM (1986) Towards a federation of broadband seismic networks. *EOS* 67: 541–542.

Roult G, Romanowicz B, and Montagner JP (1990) 3D upper mantle shear velocity and attenuation from fundamental mode free oscillation data. *Geophysical Journal International* 101: 61–80.

Romanowicz B and Snieder R (1988) A new formalism for the effect of lateral heterogeneity on normal modes and surface waves, II: General anisotropic perturbations. *Geophysical Journal of the Royal Astronomical Society* 93: 91–99.

Roult G, Rouland D, and Montagner JP (1994) Antarctica II: Upper mantle structure from velocity and anisotropy. *Physics of the Earth and Planetary Interiors* 84: 33–57.

Rumpker G and Silver PG (1998) Apparent shear-wave splitting parameters in the presence of vertically varying anisotropy. *Geophysical Journal International* 135: 790–800.

Savage MK (1999) Seismic anisotropy and mantle deformation: What have we learned from shear wave splitting? *Reviews of Geophysics* 37: 65–106.

Schlue JW and Knopoff L (1977) Shear–wave polarization anisotropy in the Pacific Ocean. *Geophysical Journal of the Royal Astronomical Society* 49: 145–165.

Sebai A, Stutzmann E, and Montagner J-P (2006) Anisotropic structure of the African upper mantle structure from Rayleigh and Love wave tomography. *Physics of the Earth and Planetary Interiors* 155: 48–62.

Shapiro NM and Ritzwoller MH (2002) Monte-Carlo inversion for a global shear-velocity model of the crust and upper mantle. *Geophysical Journal International* 151: 88–105.

Shapiro NM, Campillo M, Stehly L, and Ritzwoller MH (2005) High-resolution surface-wave tomography from ambient seismic noise. *Science* 307: 1615–1618.

Shearer PM (1991) Constrains on upper mantle discontinuities from observations of long-period reflected and converted waves. *Journal of Geophysical Research* 96: 18,147–18,182.

Sicilia D, Montagner J-P, Cara M, Debayle E, Lepine J-J, and Leveque J-J (2007) Shear-wave velocities and anisotropic structure beneath the Afar hotspot. *Tectonophysics*. (submitted).

Sieminski A, Lévêque J-J, and Debayle E (2004) Can finite-frequency effects be accounted for in ray theory surface wave tomography. *Geophysical Research Letters* 31: L24614 doi:10.129/2004GL02142.

Silveira G, Stutzmann E, Montagner J-P, and Mendes-Victor L (1998) Anisotropic tomography of the Atlantic Ocean from Rayleigh surface waves. *Physics of the Earth and Planetary Interiors* 106: 259–275.

Silveira G and Stutzmann E (2001) Anisotropic tomography of the Atlantic Ocean. *Physics of the Earth and Planetary Interiors* 132: 237–248.

Silver PG (1996) Seismic anisotropy beneath the continents: Probing the depths of geology. *Annual Review of Earth and Planetary Science* 24: 385–432.

Silver PG and Chan WW (1988) Implications for continental structure and evolution from seismic anisotropy. *Nature* 335: 34–39.

Silver PG and Holt WE (2002) The mantle flow field beneath North America. *Science* 295: 1054–1057.

Silver PG and Savage M (1994) The Interpretation of shear-wave splitting parameters in the presence of two anisotropic layers. *Geophysical Journal International* 119: 949–963.

Simons FJ, van der Hilst R, Montagner JP, and Zielhuis A (2002) Multimode Rayleigh wave inversion for shear wave speed heterogeneity and azimuthal anisotropy of the Australian upper mantle. *Geophysical Journal International* 151: 738–754.

Singh S, Taylor M, and Montagner JP (2000) On the presence of fluids in the Earth's inner core. *Science* 287: 2471–2474.

Smith SW (1986) IRIS; a program for the next decade. *EOS, Transactions of the American Geophysical Union* 67: 213–219.

Smith ML and Dahlen FA (1973) The azimuthal dependence of Love and Rayleigh wave propagation in a slightly anisotropic medium. *Journal of Geophysical Research* 78: 3321–3333.

Smith ML and Dahlen FA (1975) Correction to 'The azimuthal dependence of Love and Rayleigh wave propagation in a slightly anisotropic medium. *Journal of Geophysical Research* 80: 1923.

Smith D, Ritzwoller MH, and Shapiro NM (2004) Stratification of anisotropy in the Pacific upper mantle. *Journal of Geophysical Research* 109: B11309 doi:10.10209/2004JB03200.

Snieder R (1988) Large-scale waveform inversions of surface waves for lateral heterogeneity, 1. Theory and numerical examples. *Journal of Geophysical Research* 93: 12,055–12,066.

Snieder R, Gret A, Douma H, and Scales J (2002) Coda wave interferometry for estimating non-linear behavior in seismic velocity. *Science* 295: 2253–2255.

Solomatov VS and Moresi LN (2000) Scaling of time-dependent stagnant lid convection: Application to small-scale convection on Earth and other terrestrial planets. *Journal of Geophysical Research* 105: 21795–21817.

Spetzler J, Trampert J, and Snieder R (2002) The effect of scattering in surface wave tomography. *Geophysical Journal International* 149: 755–767.

Stutzmann E and Montagner JP (1994) Tomography of the transition zone from the inversion of higher-mode surface waves. *Physics of the Earth and Planetary Interiors* 86: 99–116.

Su W-J, Woodward RL, and Dziewonski AM (1984) Degree 12 model of shear velocity heterogeneity in the mantle. *Journal of Geophysical Research* 99: 6,945–6,980.

Su L, Park J, and Yu Y (1993) Born seismograms using coupled free oscillations: The effect of strong coupling and anisotropy. *Geophysical Journal International* 115: 849–862.

Suetsugu D and Nakanishi I (1987) Regional and azimuthal dependence of phase velocities of mantle Rayleigh waves in the Pacific Ocean. *Physics of the Earth and Planetary Interiors* 47: 230–245.

Suyehiro K, Kanazawa T, Hirata N, Shinohara M, and Kinoshita H (1992) Broadband downhole digital seismometer experiment at site 794: A technical paper. In, *Proceedings of the Ocean Drilling Project, Scientific Results*, pp. 127–128 TX: Ocean Drilling Program, College Station.

Takeuchi H and Saito M (1972) Seismic surface waves. *Methods in Computational Physics* 11: 217–295.

Tanimoto T (1986) Free oscillations in a slightly anisotropic Earth. *Geophysical Journal of the Royal Astronomical Society* 87: 493–517.

Tanimoto T (1990) Long-wavelength *S*-wave velocity structure throughout the mantle. *Geophysical Journal International* 100: 327–336.

Tanimoto T and Anderson DL (1985) Lateral heterogeneity and azimuthal anisotropy of the upper mantle: Love and Rayleigh waves. 100–250s. *Journal of Geophysical Research* 90: 1842–1858.

Tarantola A and Valette B (1982) Generalized nonlinear inverse problems solved using least squares criterion. *Reviews of Geophysics and Space Physics* 20: 219–232.

Tommasi A, Vauchez A, and Russo R (1996) Seismic anisotropy in ocean basins: Resistive drag of the sublithospheric mantle? *Geophysical Research Letters* 23: 2991–2994.

Author's personal copy

Tommasi A, Mainprice D, Canova G, and Chastel Y (2000) Viscoplastic self-consistent and equilibrium-based modeling of olivine preferred orientations. Implications for the upper mantle anisotropy. *Journal of Geophysical Research* 105: 7893–7908.

Trampert J and Snieder R (1996) Model estimations biased by truncated expansions: Possible artifacts in seismic tomography. *Science* 271: 1257–1260.

Trampert J and van Heijst HJ (2002) Global azimuthal anisotropy in the transition zone. *Science* 296: 1297–1299.

Trampert J and Woodhouse JH (2003) Global anisotropic phase velocity for fundamental mode surface waves between 40 and 150s. *Geophysical Journal International* 154: 154–165.

Tromp J, Tape C, and Liu Q (2005) Seismic tomography, adjoint methods, time reversal and banana-doughnuts kernels. *Geophysical Journal International* 160: 195–216.

Van Heijst HJ and Woodhouse JH (1997) Measuring surface-wave overtone phase velocities using a mode-branch stripping technique. *Geophysical Journal International* 131: 209–230.

Villaseñor A, Ritzwoller MH, Levshin AL, *et al.* (2001) Shear velocity structure of Central Eurasia from inversion of surface wave velocities. *Physics of the Earth and Planetary Interiors* 123: 169–184.

Vinnik LP, Chevrot S, and Montagner J-P (1998) Seismic evidence of flow at the base of the upper mantle. *Geophysical Research Letters* 25: 1995–1998.

Vinnik L, Makayeva LI, Milev A, and Usenko AY (1992) Global patterns of azimuthal anisotropy and deformations in the continental mantle. *Geophysical Journal International* 111: 433–447.

Vinnik L and Montagner J-P (1996) Shear wave splitting in the mantle from Ps phases. *Geophysical Research Letters* 23: 2449–2452.

Vinnik L, Montagner JP, Girardin N, Dricker I, and Saul J (2003) Shear wave splitting at H_2O: A comment. *Geophysical Research Letters* 30(13): 1675.

Walker KT, Bokelmann GH, and Klemperer SL (2001) Shear-wave splitting to test mantle deformation models around Hawaii. *Geophysical Research Letters* 28: 4319–4322.

Wang Z and Dahlen FA (1995) Spherical-spline parameterization of three-dimensinal earth models. *Geophysical Research Letters* 22: 3099–3102.

Wielandt E and Streickeisen G (1982) The leaf-spring seismometer: Design and performances. *Bulletin of the Seismological Society of America* 72: 2349–2367.

Wolfe CJ and Silver PC (1998) Seismic anisotropy of oceanic upper mantle. *Journal of Geophysical Research* 103: 749–771.

Wolfe CJ and Solomon SC (1998) Shear-wave splitting and implications for mantle flow beneath the melt region of the East Pacific Rise. *Science* 280: 1230–1232.

Woodhouse JH and Dziewonski AM (1984) Mapping the upper mantle: Three dimensional modelling of Earth structure by inversion of seismic waveforms. *Journal of Geophysical Research* 89: 5953–5986.

Woodhouse JH and Dahlen FA (1978) The effect of a general aspherical perturbation on the free oscillations of the Earth. *Geophysical Journal of the Royal Astronomical Society* 53: 335–354.

Woodhouse JH and Girnius (1982) Surface waves and free oscillations in a regionalized earth model. *Geophysical Journal of the Royal Astronomical Society* 68: 653–673.

Wookey J, Kendall JM, and Barruol G (2002) Mid-mantle deformation inferred from seismic anisotropy. *Nature* 415: 777–780.

Yomogida K (1992) Fresnel-zone inversion for lateral heterogeneities in the Earth. *Pure and Applied Geophysics* 138: 391–406.

Yoshizawa K and Kennett BHN (2002) Determination of the influence zone for surface wave paths. *Geophysical Journal International* 149: 441–454.

Yoshizawa K and Kennett BHN (2004) Multimode surface wave tomography for the Australian region using a three-stage approach incorporating finite frequency effects. *Journal of Geophysical Research* 109: B02310 doi:10,1029/2002JB002254.

Yu Y and Park J (1993) Anisotropy and coupled long-period surface waves. *Geophysical Journal International* 114: 473–489.

Zhang H and Thurber CH (2005) Adaptative mesh seismic tomography based on tetrahedral and Voronoi diagrams: Application to Parkfield. *Journal of Geophysical Research* 110: B04303 doi:10,129/2004JB003186.

Zhang S and Karato S-I (1995) Lattice preffered orientation of olivines aggregates deformed in simple shear. *Nature* 375: 774–777.

Zhou Y, Dahlen FA, and Nolet G (2004) Three-dimensional sensitivity kernels for surface wave observables. *Geophysical Journal International* 158: 142–168.

Zhou Y, Nolet G, Dahlen FA, and Laske G (2006) Global upper-mantle structure from finite-frequency surface-wave tomography. *Journal of Geophysical Research* 111: B04304 doi:10.1029/2005JB003677.

Relevant Websites

http://seismo.berkeley.edu – Berkeley Seismological Lab.
http://matri.ucsd.edu – Whole Eart'h Geophysics at IGPP.